

Spin-1/2 kagome Heisenberg antiferromagnet: Machine learning discovery of the spinon pair density wave ground state

Tanja Đurić, Jia Hui Chung, Bo Yang, and Pinaki Sengupta
School of Physical and Mathematical Sciences, Nanyang Technological University, 21 Nanyang Link, Singapore 637371, Singapore

(Dated: January 8, 2024)

Spin-1/2 kagome antiferromagnet (AFM) is one of the most studied models in frustrated magnetism since it is a promising candidate to host exotic spin liquid states. However, despite numerous studies using both analytical and numerical approaches, the nature of the ground state and low-energy excitations in this system remain elusive. This is related to the difficulty in determining the spin gap in various calculations. We present the results of our investigation of the Kagome AFM using the recently developed group equivariant convolutional neural networks – an advanced machine learning technique for studying strongly frustrated models. The approach, combined with variational Monte Carlo, introduces significant improvement of the achievable results accuracy in comparison with approaches based on other neural network architectures that lack generalization quality for frustrated spin systems. Contrary to the results obtained previously with various methods, that predicted Z_2 or $U(1)$ Dirac spin liquid states, our results strongly indicate that the ground state of the kagome lattice antiferromagnet is a spinon pair density wave that does not break time-reversal symmetry or any of the lattice symmetries. The found state appears due to the spinon Cooper pairing instability close to two Dirac points in the spinon energy spectrum and resembles the pair density wave state studied previously in the context of underdoped cuprate superconductors in connection with the pseudogap phase. The state has significantly lower energy than the lowest energy states found by the $SU(2)$ symmetric density matrix renormalization group calculations and other methods.

I. INTRODUCTION

Geometrically frustrated quantum magnets showed to be promising systems for discovering new phases of matter.^{1–3} Particularly interesting phases appearing in frustrated systems are various spin liquids characterized by long-range quantum entanglement, topological order and excitations with fractional quantum numbers.^{4–7} In addition to their importance in the context of high temperature superconductivity⁸ such quantum spin liquids could allow the creation of a topological qubit and have therefore been proposed as promising platforms for topological quantum computation.⁹ Kagome lattice antiferromagnets are likely candidates to host various exotic spin liquid states. However, despite numerous studies kagome antiferromagnet properties still remain unclear.

Among many numerical approaches applied to study kagome antiferromagnet properties are exact diagonalization (ED),^{10–12} density matrix renormalization group (DMRG),^{13–20} tensor network methods^{21–27} and variational Monte Carlo (VMC).^{28–39} Different studies suggested so far a variety of candidate ground states. In addition to initially proposed valence-bond crystal state with a 36-site unit cell,^{21,40–49} majority of recent DMRG and VMC studies find spin-liquid ground states. Whilst $SU(2)$ symmetric DMRG calculations obtain a fully gapped (nonchiral) Z_2 topological ground state,¹⁵ DMRG calculations supplemented with additional flux insertion indicate a gapless algebraic $U(1)$ Dirac spin liquid ground state²⁰ found also within the projected fermionic wave-function approaches^{28,29,31,35,50–53} and the tensor-network states formalism.^{25,54}

Difficulty in finding quantum spin liquids in realistic microscopic models is largely due to lack of adequate unbiased computational methods. Unbiased quantum Monte Carlo simulations face still unsolved sign problem^{55,56} while tensor network and many variational approaches are often biased towards particular kinds of states. Also, although DMRG method^{57–60} is known to be very accurate method for calculating properties of one-dimensional systems, difficulty of obtaining reliable results with DMRG greatly increases for D -dimensional systems with $D > 1$. In addition, matrix product states within DMRG algorithm are biased towards low-entangled wave-functions.⁶¹ Gapped low-entangled states are therefore more favored within DMRG algorithm than highly entangled gapless phases.

Moreover, it has been found that two-dimensional gapless spin liquid states are particularly delicate states of matter that can be destabilized on constrained geometries like DMRG cylinders.⁶² The ground-state properties for DMRG cylinders can therefore be very different from the ground-state properties for the truly two-dimensional lattices. An important step in the direction of avoiding possible destabilization of gapless spin liquid states in DMRG calculations was achieved by including fictitious magnetic fluxes in the original spin model. This flux threading through DMRG cylinders allowed detection of possible gapless $U(1)$ spin liquid ground states and Dirac points in the excitation spectrum in the kagome and triangular lattices.^{20,63,64}

In our calculations we employ advanced neural networks based machine learning (ML) techniques to study properties of the kagome lattice antiferromagnet since these novel unbiased ML techniques have so far

shown great promise and potential for studying various many-body problems. An important advantage of the ML approach is suitability for implementation on graphics processing units (GPUs) that have enhanced computational capability. Namely, GPUs can perform multiple simultaneous computations and provide significant computational process speedup. Additional benefit is also powerful ML optimization libraries like NetKet^{65,66} and TensorFlow⁶⁷ libraries.

Neural network quantum states (NQS) have recently been recognized as powerful variational wave-function ansätze that allow accurate representation of various quantum many-body states. Carleo and Troyer proposed an NQS ansatz based on the restricted Boltzmann machine neural network⁶⁸ that was initially introduced for quantum spin systems without geometrical frustration. The applicability of various NQS ansätze has later been extended to many complex challenging many-body problems for which the exact solutions are still not known. Among many examples are frustrated spin systems,^{36–39,69–81} fermionic models^{69,82–87} and topological phases of matter.^{88–96} In addition to the initial NQS based calculations that considered mainly ground-state properties, neural network based numerical methods have also been further developed to study excited energy states,^{76,78,80–82,95–98} time dynamics of many-body quantum systems,^{99–101} open quantum systems^{102–107} and thermal quantum states at finite temperatures.^{108,109}

Several recent studies showed that accuracy and performance of the NQS based methods can be significantly improved by restoring symmetries in variational NQS ansätze via quantum-number projections,^{73,74,76,78,82,98,110–113} introduction of equivariant models for various symmetry groups^{80,81,84,114–117} or transformation to basis of irreducible representations for quantum states with nonabelian or anyonic symmetries.^{95,96} Equivariance based symmetrization combined with deep neural network ansätze demonstrated so far significant advantage in comparison to other symmetry averaging procedures allowing high-accuracy variational Monte Carlo calculations for highly frustrated quantum magnets. Notably, Roth, Szabó and MacDonald recently obtained very accurate results for J_1 - J_2 Heisenberg models on the square and triangular lattices.^{80,81}

We study properties of the spin-1/2 kagome lattice antiferromagnet by representing the ground and low-lying excited energy states by group equivariant convolutional neural network (GCNN) ansätze equivariant over the full space group composed of transformations that leave the kagome lattice unchanged (lattice translations and dihedral $D(6)$ point group transformations). In addition of being very expressive ansätze GCNN also possess greater ability to learn from a limited number of samples, that is greater generalization quality, in comparison with other neural network architectures. This improved generalization quality allows more efficient neural network training yielding to significant improvement of the achievable

results accuracy within the GCNN approach combined with VMC. Unlike density matrix renormalization group and other variational methods including tensor network approaches, the GCNN and VMC approach does not exhibit significant bias towards any particular kind of states and therefore provides an important step in clarifying the kagome antiferromagnet properties and a reference to check validity of the results obtained with other methods.

Our numerical calculations were performed on NVIDIA A100 80GB GPUs and using NetKet,^{65,66} JAX,¹¹⁸ FLAX,¹¹⁹ and OPTAX¹²⁰ libraries. Contrary to the results obtained previously with other methods, we find that the kagome lattice antiferromagnet ground state is a spinon pair density wave (PDW) state that does not break time-reversal symmetry or any of the lattice symmetries. The state appears due to the spinon Cooper pairing instability close to two Dirac nodes of the underlying $U(1)$ Dirac spin liquid found with recent flux insertion supplemented DMRG approach²⁰ and also with projected fermionic wave-function approaches^{28,29,31,35,50–53} and within the tensor-network states formalism.^{25,54} The found spinon PDW resembles the pair density wave state studied previously in the context of underdoped cuprate superconductors in connection with pseudogap phase^{121–125} and has significantly lower energy than the ground state energy values obtained by other methods. In particular, for the studied system sizes we find that the PDW energy has $\approx 1.78\%$ lower value than the ground state energy found by $SU(2)$ symmetric density matrix renormalization group calculations.¹⁵

The paper is organized as follows. In Sec. II we describe the GCNN wave-function ansätze. In Sec. III we explain wave-function optimization procedure. Our results for the ground state properties and low-energy excited states are presented in Sec. IV. We summarize our results, draw conclusions and discuss future research directions in the last section, Sec. V.

II. WAVE-FUNCTION REPRESENTATION WITH GROUP CONVOLUTIONAL NEURAL NETWORKS

Deep neural networks, and in particular deep convolutional neural networks (CNNs), have proven to be very powerful models for pattern recognition in image, video and audio data analysis,^{126–128} with both depth and convolutional weight sharing playing important role in the predictive power of these models. Convolutional weight sharing, that is, using the same weights to model for example different parts of an image, provides an effective description due to the presence of translational symmetry (up to edge effects) in most of the mentioned pattern recognition tasks. CNNs therefore use significantly smaller number of parameters than fully connected networks while preserving expressivity and capacity to learn useful features. Since quantum many-body wavefunc-

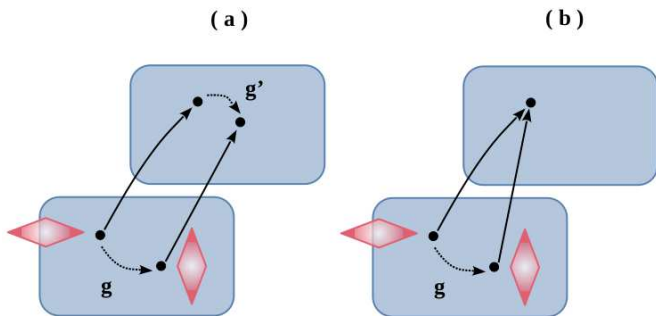


FIG. 1: Schematic illustration of (a) equivariance: $f(gx) = g'f(x)$, and (b) invariance: $f(gx) = f(x)$.

tions for various lattice Hamiltonians similarly often possess translational symmetry, CNN based NQS ansätze allow efficient representation of these wavefunctions.

CNNs can be generalized to take into account all relevant lattice symmetries. GCNNs^{80,81,117,129} are such CNN generalizations to arbitrary nonabelian groups that take into account all space-group symmetries. Space-group symmetries in general include both lattice translations and all lattice point-group symmetries such as rotations and reflections. The key property of CNNs and GCNNs is equivariance of the convolution layers where increasingly abstract representations of the input are developed by alternating convolution operations with nonlinearities. The equivariance property is the only property required to specify symmetry eigenvalues.

With a symmetry group denoted by G , input denoted by x and transformations that correspond to the group elements by g , a function, layer or network f is equivariant with respect to the transformations g if

$$f(gx) = g'(f(x)) \quad (1)$$

for any g , where g and g' do not in general need to be the same. As illustrated in FIG. 1 invariance is obtained if g' is identity map for all transformations g . In other words, f preserves the symmetry group structure in the sense that acting on inputs by symmetry transformations causes outputs to be transformed by the same symmetry elements in a non-trivial way.

For systems of interacting spins on a lattice neural network ansätze for the wavefunctions $|\psi\rangle$ of the lattice Hamiltonian associate a complex number $\psi(\vec{\sigma}; \vec{\alpha})$ with each computational basis configuration of spins $|\vec{\sigma}\rangle$ where $\vec{\alpha}$ denotes the network parameters:

$$|\psi\rangle = \sum_{\{\vec{\sigma}\}} \psi(\vec{\sigma}; \vec{\alpha}) |\vec{\sigma}\rangle, \quad (2)$$

and $\vec{\sigma} = \{\sigma(\vec{r}_1), \dots, \sigma(\vec{r}_N)\}$ with $\vec{r}_1, \dots, \vec{r}_N$ being positions of the lattice sites. In other words, spin configurations $|\vec{\sigma}\rangle$ are the network inputs, and the complex coefficients $\psi(\vec{\sigma})$ are the network outputs as illustrated in FIG. 2.

For example, for a square lattice with periodic bound-

ary conditions a CNN convolutional mapping is

$$\psi(\vec{r}) = \sum_{\vec{r}'} K(\vec{r} - \vec{r}') \sigma(\vec{r}'), \quad (3)$$

where K is an arbitrary kernel matrix that looks for and filters patterns in $\vec{\sigma}$. The mapping is clearly translation equivariant since

$$\begin{aligned} \sum_{\vec{r}'} K(\vec{r} - \vec{r}') \sigma(\vec{r}' + \vec{t}) &= \sum_{\vec{r}'} K(\vec{r} + \vec{t} - \vec{r}') \sigma(\vec{r}') \\ &= \psi(\vec{r} + \vec{t}). \end{aligned} \quad (4)$$

It can similarly be shown that several iterations of convolutional mappings of the form (3) combined with arbitrary pointwise non-linear functions, and therefore neural networks built from layers of such mappings, are also translation equivariant. A translation for \vec{t} acts by adding \vec{t} to both input and output coordinates and shifting input data and then passing the data through a number of layers is the same as passing the original data through the same layers and then shifting the resulting output feature maps.

In GCNNs convolutions of the form (3) are generalized to arbitrary discrete nonabelian groups. For a symmetry group G with elements \hat{g} an embedding layer first generates feature maps from the input data

$$\mathbf{f}_g^1 = \Gamma \left(\sum_{\vec{r}} \mathbf{K}(\hat{g}^{-1}\vec{r}) \sigma(\vec{r}) \right) \quad (5)$$

for a set of learnable kernels or filters \mathbf{K} that extract local features from the input and Γ is a non-linear activation function. The output of the embedding layer is further passed to any number of group convolutional layers denoted by $i = 2, \dots, N_l$ where feature to feature convolutions are performed as

$$\mathbf{f}_g^{i+1} = \Gamma \left(\sum_{\hat{h} \in G} \mathbf{W}^i(\hat{h}^{-1}\hat{g}) \mathbf{f}_h^i \right) \quad (6)$$

for a set of convolutional kernels \mathbf{W} . Depth of the filters \mathbf{K} is one (the same depth as input data) and depth of the filters \mathbf{W}^i equals to the number of feature maps in the i -th layer. Here Γ is taken to be scaled exponential



FIG. 2: Spin configurations $|\vec{\sigma}\rangle$ are GCNN inputs, and the complex ansatz wave-function coefficients $\psi(\vec{\sigma})$ GCNN outputs.

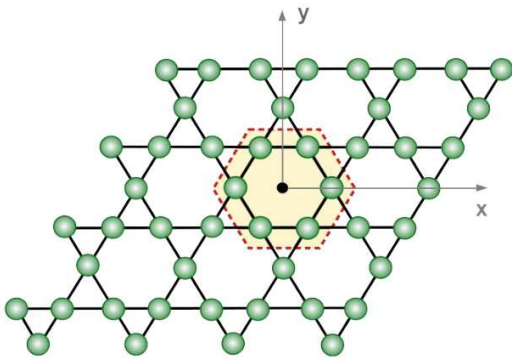


FIG. 3: Local cluster for which elements of the embedding kernels K are nonzero. The $\vec{r} = (0, 0)$ point is the origin for lattice sites and $D(6)$ point group symmetries.

linear unit (SELU) activation function:

$$\text{SELU}(x) = a \begin{cases} x & x > 0 \\ b(e^x - 1) & x \leq 0 \end{cases} \quad (7)$$

with $a \approx 1.05$ and $b \approx 1.67$, and applied separately to the real and imaginary components:

$$\Gamma(x) = \text{SELU}(\text{Re}(x)) + i\text{SELU}(\text{Im}(x)). \quad (8)$$

The SELU activation functions were introduced for self-normalizing neural networks¹³⁰ since these activations generate self-normalizing properties, namely variance stabilization that helps in avoiding exploding and vanishing gradients when training deep neural networks, i.e. when optimizing variational wave function parameters. The SELU nonlinearity moves distribution of the nonlinearity inputs for the network layers towards mean being zero and variance one allowing stable training for very deep neural networks.

All N_l hidden layers are followed by the Γ activation function. To obtain $\psi(\vec{\sigma})$ in equation (2) the final output layer exponentiates complex-valued feature maps composed of two real-valued feature maps, calculates sum of these exponentiated values, and projects the sum on a particular irreducible representation of the symmetry group G that corresponds to the symmetry properties of the ansatz wavefunction:

$$\psi(\vec{\sigma}) = \sum_{\hat{g} \in G} \chi_{\hat{g}}^* \sum_{n=1}^{N_f} \exp(f_{n,\hat{g}}^{N_l}) \quad (9)$$

where N_f is the number of complex-valued feature maps (composed of $2 \cdot N_f$ real-valued feature maps) in the N_l -th layer and $\chi_{\hat{g}}$ are characters of the irreducible representation.^{131,132} The nonlinear activation function before the output is taken to be identity function.

Within group theory representations are eigenfunctions of the symmetry group operations. Irreducible representations are eigenfunctions of all group operations whilst reducible representations are eigenfunctions only

of a subset of these operations. Each irreducible representation has different set of eigenvalues. These eigenvalues are characters χ_g in the equation (9). For non-degenerate symmetry groups where every irreducible representation consists of one eigenfunction, characters are $+1$ or -1 , whilst for degenerate symmetry groups characters can differ from ± 1 .

Described GCNN models are significantly more expressive and yield more accurate results than standard symmetry-averaged models obtained by applying the projection formula.^{131,132}

$$|\psi\rangle = \frac{d_\chi}{|G|} \sum_{\hat{g} \in G} \chi_{\hat{g}}^* \hat{g} |\tilde{\psi}\rangle, \quad (10)$$

$$\psi(\vec{\sigma}) = \frac{d_\chi}{|G|} \sum_{\hat{g} \in G} \chi_{\hat{g}}^* \tilde{\psi}(\hat{g}^{-1}\vec{\sigma}),$$

where $|G|$ is the order of the group G (the number of its elements) and d_χ is dimension of the irreducible representation with characters χ_g . The projection symmetry averaging approach has been applied to various ansatz wavefunctions^{71,76,78,111,113} and requires evaluation of the model $\tilde{\psi}$ for all symmetry related basis states which can be very computationally expensive. These models are also equivariant with respect to the symmetry group G which can be seen by rewriting an ansatz of the form (10) as an equivariant model with the output dimension $|G|$:

$$\begin{aligned} \psi_g(\vec{\sigma}) &\equiv \tilde{\psi}(\hat{g}^{-1}\vec{\sigma}), \\ \psi_g(\hat{h}^{-1}\vec{\sigma}) &= \tilde{\psi}(\hat{g}^{-1}\hat{h}^{-1}\vec{\sigma}) = \psi_{hg}(\vec{\sigma}). \end{aligned} \quad (11)$$

Within this formulation all $\psi_g(\vec{\sigma})$ can be obtained by evaluating the equivariant model for a single input and symmetrization is equivalent to averaging over the model output which is computationally preferable.

For example, for the simpler square lattice with periodic boundary conditions the projection formula (10) becomes familiar Fourier transform that finds crystal momentum eigenstates:

$$\psi(\vec{\sigma}) = \frac{1}{L_x \cdot L_y} \sum_{\vec{r}} e^{-i\vec{k} \cdot \vec{r}} \psi_{\vec{r}}(\vec{\sigma}), \quad (12)$$

with L_x and L_y being the lattice dimensions and $\vec{k} = 2\pi \cdot (n_x/L_x, n_y/L_y)$, $n_q \in \{0, \dots, L_q - 1\}$, $q \in \{x, y\}$. Irreducible representations of the translation group are therefore one-dimensional and can be labeled by the phases $e^{i\vec{k} \cdot \vec{r}}$.

GCNNs can be mapped to other deep neural network models with symmetry averaging by masking filters, i.e. by setting various off-diagonal feature-to-feature filters (convolution kernels W) to zero whilst keeping the input-to-feature filters (embedding kernels K) the same.^{80,81} Diagonal filters are filters with $\hat{h} = \hat{g}$ in (6) and off-diagonal filters are obtained for $\hat{h} \neq \hat{g}$. For example

translationally equivariant CNN model symmetry averaged over a lattice point group symmetries can be obtained by masking off-diagonal filters that correspond to point group rotations and reflections. This model would be more restrictive than a GCNN model equivariant with respect to all space-group symmetries yielding less accurate results.^{80,81,117}

We also note that using local embedding kernels K , obtained by restricting nonzero K elements only to local clusters, stabilizes the optimization procedure and allows numerical calculations with deeper neural networks.^{80,81} The optimization procedure, i.e. the network training where the network learns from the feedback from variational principle, has faster convergence for GCNN architectures with local kernels since the kernel locality structures the representation of long-range correlations and simplifies the learning landscape. Locality in the convolutional kernels W is imposed by restricting the kernels to the symmetry operations of the form $\hat{g} = \hat{t}\hat{p}$ where \hat{t} is a lattice translation and \hat{p} is a lattice point-group symmetry operation.

In our calculations for the kagome antiferromagnet kernels K are restricted to the symmetric local cluster illustrated in FIG. 3. We find that choosing larger clusters with different symmetric shapes does not improve convergence nor stability of the algorithm. Set of the crystal momenta related to the lattice translations and the lattice Brillouin zone are illustrated in FIG. 4. Positions of the kagome lattice sites are $\vec{R}_{L_1, L_2, k} = L_1 \cdot \vec{a}_1 + L_2 \cdot \vec{a}_2 + \vec{r}_k$ where $\vec{a}_1 = (1, 0)$ and $\vec{a}_2 = (1/2, \sqrt{3}/2)$ are two primitive vectors of the lattice unit cell containing three inequivalent sites, and \vec{r}_k describe positions of the sites within the unit cell: $\vec{r}_1 = (1/2, 0)$, $\vec{r}_2 = (1/4, \sqrt{3}/4)$ and $\vec{r}_3 = (3/4, \sqrt{3}/4)$. Two primitive basis vectors $\vec{b}_1 = 2\pi(1, -1/\sqrt{3})$ and $\vec{b}_2 = 4\pi(0, 1/\sqrt{3})$ in the reciprocal lattice are calculated as $\vec{b}_1 = 2\pi \frac{\hat{O}_R \vec{a}_2}{\vec{a}_1 \cdot \hat{O}_R \vec{a}_2}$ and $\vec{b}_2 = 2\pi \frac{\hat{O}_R \vec{a}_1}{\vec{a}_2 \cdot \hat{O}_R \vec{a}_1}$ where \hat{O}_R represents $\pi/2$ (anti-clockwise)

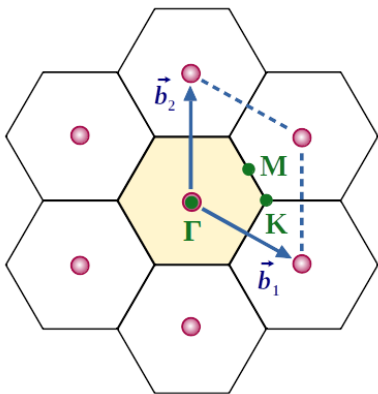


FIG. 4: High symmetry points (Γ , M and K) in the kagome lattice Brillouin zone where \vec{b}_1 and \vec{b}_2 are two primitive basis vectors in the reciprocal lattice.

rotation matrix.

Our calculations have been performed with GCNN ansätze having 6 layers and 6 feature maps in each layer for the kagome lattice cluster with 48 lattice sites and GCNN ansätze having 4 layers and 4 feature maps in each layer for the kagome lattice cluster with 108 lattice sites. In addition to the space-group symmetry, composed of lattice translations and dihedral $D(6)$ point group transformations, the total symmetry group for the ansätze also includes \mathbb{Z}_2 spin parity group generated by $P_{\mathbb{Z}_2} = \prod_i \sigma_i^x$ for the eigenstates with $M_z = \sum_{i=1}^N \sigma(\vec{r}_i) = 0$ where $\sigma(\vec{r}_i) \in \{-1/2, 1/2\}$ and N is the number of lattice sites. Irreducible representations of the spin parity group are specified by the eigenvalues of $P_{\mathbb{Z}_2}$ which can be $+1$ or -1 . Total spin quantum number for an eigenvalue $|\psi_{P_{\mathbb{Z}_2}}\rangle$ that is also an eigenvalue of the total spin operator can be obtained by calculating $\langle \psi_{P_{\mathbb{Z}_2}} | \hat{S}_{tot}^2 | \psi_{P_{\mathbb{Z}_2}} \rangle$. The total spin operator is $\hat{S}_{tot} = (\hat{S}_{tot}^x, \hat{S}_{tot}^y, \hat{S}_{tot}^z)$ where $\hat{S}_{tot}^q = \sum_{i=1}^N \hat{S}_i^q$ with $q \in \{x, y, z\}$ and $\hat{S}_{tot}^2 |\psi_S\rangle = S(S+1) |\psi_S\rangle$ where $|\psi_S\rangle$ is an eigenstate with total spin quantum number S .

Described procedure of constructing the wave-function ansätze equivariant with respect to a discrete symmetry group cannot straightforwardly be generalized to continuous symmetry groups like $SU(2)$ spin rotation symmetry. Finding efficient ways to introduce continuous symmetries is still an open research problem with one of the possible solutions being sampling in the basis of irreducible representations instead of spins.^{95,96,111}

III. TRAINING SCHEME AND WAVE-FUNCTION OPTIMIZATION

Within the VMC approach variational wavefunctions described by GCNN ansätze are optimized using stochastic reconfiguration method introduced by Sorella *et al.*^{133–136} The goal of VMC is to find the optimal set of (complex) parameters $\vec{\alpha} = \{\alpha_1, \dots, \alpha_{N_p}\}$ in an ansatz wavefunction of the form (2) that minimizes a suitably chosen loss function. The standard optimization technique is the gradient descent (GD) method within which the parameters are updated according to the gradients of the chosen loss function with the iterative update rule

$$\vec{\alpha}_{t+1} = \vec{\alpha}_t - \eta \vec{\nabla}_{\vec{\alpha}} \mathcal{L}, \quad (13)$$

where t denotes iteration, η is the learning rate (the step size) and \mathcal{L} is the loss function. All numerical methods that attempt to find a global minimum using local information for iterative parameter updates generally exhibit problems related to the local minima in the loss function landscape and slow convergence. Various stochastic methods are therefore introduced to help mentioned numerical algorithms to escape local minima and improve convergence, for example Adam¹³⁷ and natural gradient descent (NGD) method.^{138–143}

In the equation (13) $-\vec{\nabla}_{\vec{\alpha}}\mathcal{L}$ represent directions in which the parameters can be updated to obtain the largest decrease of the loss function. The parameters are adjusted by a small step length, i.e. moved for a small distance in the parameter space, in the direction determined by the gradient to optimize the loss function. The standard GD and NGD methods differ by how a small distance is defined. Whilst in the standard GD distance is Euclidean distance that corresponds to the flat metric on the parameter manifold, NGD replaces the flat metric by a generally non-flat metric. NGD method takes into account that changes of all parameters can not be treated equally and that it is not always correct to define distance in terms of how much the parameters are adjusted. Instead a change for each parameter has to be scaled according to the effect of the change on the neural network output distribution.

To define a new form of distance that accounts for relationships between parameters and reflects changes in the network output distribution NGD method introduces a metric matrix M

$$\vec{\alpha}_{t+1} = \vec{\alpha}_t - \eta M^{-1} \vec{\nabla}_{\vec{\alpha}} \mathcal{L}, \quad (14)$$

In the context of VMC with neural networks NGD method corresponds to the stochastic reconfiguration method (SR),^{68,133–136,143} where the Hilbert-space distance d between two unnormalized wavefunctions $|\phi\rangle$ and $|\phi'\rangle$ is given by the Fubini-Study metrics:

$$d_{FS} = \arccos \sqrt{\frac{\langle \phi' | \phi \rangle \langle \phi | \phi' \rangle}{\langle \phi' | \phi' \rangle \langle \phi | \phi \rangle}}. \quad (15)$$

Within SR the parameter updates (14) at each iteration t can be obtained by applying imaginary time evolution operator $e^{-\Delta\tau\mathcal{L}} \approx 1 - \Delta\tau\mathcal{L}$ to the ansatz wavefunction at imaginary time τ :

$$|\psi'(\vec{\alpha}(\tau))\rangle = (1 - \Delta\tau\mathcal{L}) |\psi(\vec{\alpha}(\tau))\rangle, \quad (16)$$

where $\Delta\tau$ is a small imaginary time step that corresponds to the learning rate η in the equation (14). After each imaginary time step $\Delta\tau$ the wavefunction $|\psi'(\vec{\alpha}(\tau))\rangle$ is projected to the variational subspace by minimizing d_{FS}^2 with $|\phi\rangle = |\psi(\vec{\alpha}(\tau))\rangle + \Delta\tau\partial_\tau\psi(\vec{\alpha}(\tau))$ and $|\phi'\rangle = |\psi'(\vec{\alpha}(\tau))\rangle$ in the equation (15) to obtain a new set of parameters $\vec{\alpha}_{t+1} \equiv \vec{\alpha}(\tau + \Delta\tau)$:

$$\vec{\alpha}_{t+1} = \vec{\alpha}_t - \Delta\tau G^{-1} \vec{\nabla}_{\vec{\alpha}} \mathcal{L}, \quad (17)$$

where the metric matrix M corresponds to the quantum geometric tensor (QGT):

$$G_{ij} = \frac{\langle \partial_{\alpha_i} \psi(\vec{\alpha}) | \partial_{\alpha_j} \psi(\vec{\alpha}) \rangle}{\langle \psi(\vec{\alpha}) | \psi(\vec{\alpha}) \rangle} - \frac{\langle \partial_{\alpha_i} \psi(\vec{\alpha}) | \psi(\vec{\alpha}) \rangle \langle \psi(\vec{\alpha}) | \partial_{\alpha_j} \psi(\vec{\alpha}) \rangle}{\langle \psi(\vec{\alpha}) | \psi(\vec{\alpha}) \rangle^2}, \quad (18)$$

and $\partial_{\alpha_i} = \partial/\partial\alpha_i$ are partial derivatives with respect to the network parameters $\vec{\alpha} = \{\alpha_1, \dots, \alpha_{N_p}\}$. The QGT

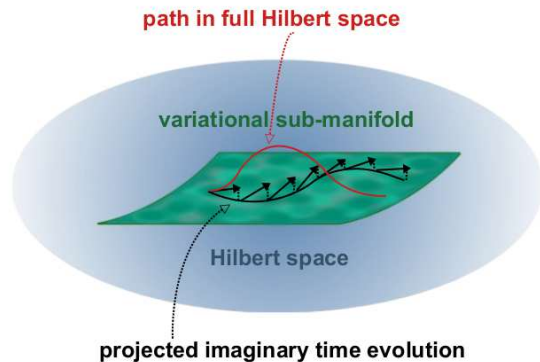


FIG. 5: Schematic illustration of the imaginary time evolution in the stochastic reconfiguration method. Starting from a variational wavefunction $|\psi(\vec{\alpha})\rangle$ with parameters $\vec{\alpha}$ application of the imaginary time evolution operator $e^{-\delta\tau\mathcal{L}} \approx 1 - \Delta\tau\mathcal{L}$ with a small imaginary time step $\Delta\tau$ results in the wavefunction $|\psi'(\vec{\alpha})\rangle = (1 - \Delta\tau\mathcal{L})|\psi(\vec{\alpha})\rangle$ (black arrows). After each imaginary time step $\Delta\tau$ the wavefunction $|\psi'(\vec{\alpha})\rangle$ is projected to the variational subspace by minimizing the distance d_{FS}^2 (15) between $|\psi'(\vec{\alpha})\rangle$ and $|\psi(\vec{\alpha}')\rangle$ to obtain new updated set of parameters $\vec{\alpha}'$.

is also often called the S matrix or quantum Fisher matrix in analogy to the classical Fisher information matrix.^{65,66,138,142,143} Schematic illustration of the imaginary time evolution in the SR method is shown in FIG. 5.

The most often choice of the loss function in VMC is the variational energy:

$$\mathcal{L}_E \equiv E = \frac{\langle \psi(\vec{\alpha}) | H | \psi(\vec{\alpha}) \rangle}{\langle \psi(\vec{\alpha}) | \psi(\vec{\alpha}) \rangle}. \quad (19)$$

where H is the Hamiltonian of the system. For the kagome lattice antiferromagnet the Heisenberg Hamiltonian is

$$H = J \sum_{\langle i,j \rangle} \vec{S}_i \cdot \vec{S}_j, \quad (20)$$

where the exchange coupling $J > 0$ and $\langle i,j \rangle$ denotes all possible nearest-neighboring (NN) pairs of the kagome lattice sites and the spin 1/2 operators $\hat{S}_i = \frac{1}{2}(\hat{\sigma}^x, \hat{\sigma}^y, \hat{\sigma}^z)$ can be written in terms of the Pauli matrices $\hat{\sigma}_i$ with $i \in \{x, y, z\}$.

Eq.(17) is however ill-conditioned, meaning that a small error in the energy gradients may cause a large error in the parameter updates. Also the QGT matrix G can be non-invertible. The G matrix regularization is therefore required to stabilize calculations and to achieve reliable convergence. We find that adding both a scale-invariant shift ϵ_1 and a constant shift ϵ_2 to diagonal entries

$$G_{ii} \rightarrow G_{ii} + \epsilon_1 G_{ii} + \epsilon_2 \quad (21)$$

provides suitable regularization at the later stages of the calculations when the variational energy is relatively close to the ground state energy. However the mentioned regularization scheme is often unstable at the beginning of the network training exhibiting run-away-like instabilities typical for non-stoquastic quantum Hamiltonians with rugged variational manifold landscape.⁷⁹ For GCNN architectures similar behavior was previously noticed in studies of the frustrated J_1 - J_2 model.^{80,81}

The instability problem at the initial stages of the training can be remedied by modifying considered loss function, that is by reshaping the optimization landscape, as it was demonstrated in several recent studies considering other complex models.^{80,81,144–147} Adding a pseudo-entropy reward term with an effective temperature T to the energy loss function encourages more even sampling of the Hilbert space and leads to the total loss function:

$$\mathcal{L}_F \equiv F = E - TS, \quad (22)$$

corresponding to free energy at the temperature T where the entropy is defined as^{80,81,144–147}

$$S = - \sum_{\vec{\sigma}} \frac{|\psi(\vec{\sigma}, \vec{\alpha})|^2}{\sum_{\vec{\sigma}'} |\psi(\vec{\sigma}', \vec{\alpha})|^2} \log \frac{|\psi(\vec{\sigma}, \vec{\alpha})|^2}{\sum_{\vec{\sigma}'} |\psi(\vec{\sigma}', \vec{\alpha})|^2}, \quad (23)$$

and $\psi(\vec{\sigma}, \vec{\alpha})$ is an unnormalized neural-network ansatz wavefunction. Within this approach the effective temperature is set to some initial $T = T_0$ at the start of the training and then gradually lowered to zero as the training proceeds according to a schedule function T_n for the effective temperature in the n -th training step.

Similarly as for the J_1 - J_2 model,^{80,81} in our kagome lattice antiferromagnet study the function T_n of the form $T_n = T_0 e^{-\lambda n}$ with $T_0 = 0.5$ and $\lambda = 0.02$ the most effectively solves the problem with initial instabilities for a range of random initial parameter values. We however note that for larger lattice sizes we still find residual instabilities for some initial random parameter values that are prone to the instabilities and lead to unstable trajectories in the network parameters manifold. This dependence on the initial parameter values can in general appear for non-stoquastic quantum Hamiltonians in rugged neural network landscapes.⁷⁹ The sum in Eq.(22) is over all basis states $\vec{\sigma}$ and at large values of T at the beginning of the training the network tries to first learn states with similar amplitudes for all basis states. This in addition to the training stabilization also significantly increases achievable results accuracy which is consistent with findings in several previous neural network studies that indicate improved algorithm performance with including pre-training of the phases.^{75,80}

We also point out that minimizing the free energy loss function (22) is equivalent to minimizing Kullback-Leibler (KL) divergence that measures closeness between two distributions. For a statistical physics model the joint probability for spins $\vec{\sigma} = \{\sigma_1, \dots, \sigma_N\}$ follows the

Boltzmann distribution

$$p(\vec{\sigma}) = \frac{e^{-\beta E(\vec{\sigma})}}{Z}, \quad (24)$$

where $\beta = 1/T$ is the inverse temperature and Z is the partition function and the free energy \mathcal{F} can be obtained as $\mathcal{F} = -\ln Z/\beta$. The KL divergence¹⁴⁸

$$D_{KL} = \sum_{\vec{\sigma}} \psi(\vec{\alpha}, \vec{\sigma}) \ln \left(\frac{\psi(\vec{\alpha}, \vec{\sigma})}{p(\vec{\sigma})} \right) = \beta(F - \mathcal{F}) \quad (25)$$

then measures closeness between the Boltzmann distribution $p(\vec{\sigma})$ and $\psi(\vec{\alpha}, \vec{\sigma})$ distribution parameterized by variational parameters $\vec{\alpha}$ where

$$F = \frac{1}{\beta} \sum_{\vec{\sigma}} \psi(\vec{\alpha}, \vec{\sigma}) [\beta E(\vec{\sigma}) + \ln \psi(\vec{\alpha}, \vec{\sigma})] \quad (26)$$

is the variational free energy that gives an upper bound for the free energy \mathcal{F} . Since the KL divergence is non-negative, KL minimization is equivalent to the free energy loss (22) minimization.

IV. LOW-LYING ENERGY STATES AND GROUND STATE PROPERTIES

In this section we present results for the ground state properties and low-lying eigenstates in the energy spectrum for the kagome lattice antiferromagnet clusters with 48 ($4 \times 4 \times 3$) and 108 ($6 \times 6 \times 3$) lattice sites and periodic boundary conditions. Whilst the ground state for the smaller lattice size is fully symmetric, we demonstrate further in the section that the ground state for larger cluster with 108 sites is in a nontrivial symmetry sector with nonzero lattice momentum revealing its long-range entanglement,¹⁴⁹ presence of Dirac points in the energy spectrum and instability towards spinon Cooper pair formation. We note that previous DMRG studies also found indications of the possible spinon Cooper pairing instability. In particular DMRG calculations¹⁴ found that the triplet excitations appear to be composed of two spinons, however could not resolve whether two spinons bind or not on studied cylindrical geometries.

The space group for the $N_1 \times N_2 \times 3$ kagome lattice clusters with $N_1 = N_2 = L$ and periodic boundary conditions contains $12 \times L^2$ symmetry operations obtained by combining L^2 lattice translations and 12 D(6) point group symmetries (rotations and reflections). The space group irreducible representations are usually constructed and described in terms of a set of symmetry related crystal momenta called star, and a subgroup of the point group called little group that leaves these symmetry related crystal momenta invariant.¹⁵⁰

For the cluster with 48 sites ED calculations¹⁰ found that the ground state is fully symmetric corresponding to the symmetry sector with all discrete space-group symmetry characters $\chi_g = 1$. The state is in the total $S = 0$

D(6)	e	R ³	R	R ²	τ	τR
χ_0	1	1	1	1	1	1
χ_1	1	1	1	1	-1	-1
χ_2	1	-1	-1	1	1	-1
χ_3	1	-1	-1	1	-1	1
χ_4	2	-2	1	-1	0	0
χ_5	2	2	-1	-1	0	0

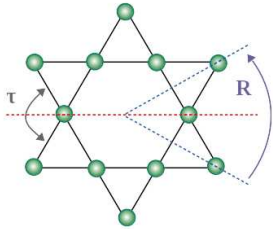


FIG. 6: Generators of the kagome lattice point group $D(6)$: (anticlockwise) rotation for $\pi/3$ around the center of the hexagonal plaquette and reflection mapping $y \rightarrow -y$. The table shows group elements of the little group for the crystal momentum $\vec{q} = (0, 0)$ (Γ high symmetry point in the kagome lattice Brillouin zone) and corresponding irreducible representation characters. $D(6)$ point group contains 12 elements corresponding to 12 point group symmetry operations (6 rotations and 6 reflections). The little group is a subgroup of $D(6)$ that leaves the crystal momentum invariant.

sector with spin parity $P_{Z_2} = 1$. As illustrated in FIG. 6, the space-group characters can be obtained from the χ_0 characters of the little group for the crystal momentum $\vec{q} = (0, 0)$ of the Γ high symmetry point in the kagome lattice Brillouin zone shown in FIG. 4 (further denoted by χ_0^0).

The first higher energy state in the total $S = 0$ sector for 48 sites cluster also has spin parity $P_{Z_2} = 1$ and is characterized with the crystal momentum $\vec{q} = (0, 0)$ (Γ high symmetry point), however with the π -rotation eigenvalue -1 according to ED calculations.¹⁰ We find that the corresponding wavefunction transforms as the irreducible representation of the space group constructed from the little group irreducible representations for the crystal momentum $\vec{k} = (0, 0)$ described by characters χ_2 in FIG. 6. The space-group characters in this symmetry sector are further denoted by χ_0^1 .

Furthermore, ED studies found that the lowest energy state in the total $S = 1$ sector for 48 sites cluster has spin parity $P_{Z_2} = -1$, π -rotation eigenvalue -1 and finite crystal momentum $\vec{q} = (\pi, \pi/\sqrt{3})$.¹⁰ The wavefunction is found to transform according to the irreducible representation of the space group constructed from the little group irreducible representation for the crystal momentum $\vec{q} = (\pi, \pi/\sqrt{3})$ (M high symmetry point in the kagome lattice Brillouin zone shown in FIG. 4) described by characters χ_2 in FIG. 7. We denote space-group characters for this symmetry sector by χ_1^0 .

To check accuracy of the GCNN and VMC approach we first calculate the ground state energy and singlet and triplet energy gaps for 48 sites kagome lattice cluster. The singlet excitation gap $\Delta_s = E_1(S = 0) - E_0(S = 0)$ is defined as energy difference of the two lowest energy states in the total spin $S = 0$ sector, whilst the triplet

spin excitation gap $\Delta_t = E_0(S = 1) - E_0(S = 0)$ can be obtained as energy difference of the lowest energy states in the total spin $S = 1$ and $S = 0$ sectors.

First the ground state energy is found by minimizing the free energy loss (22) with fully symmetric wavefunction ansatz with space-group characters χ_0^0 and spin parity $P = 1$ using SR optimization algorithm and the low-lying excited states are further found using transfer learning approach. Namely to stabilize and expedite training within SR optimization for the lowest energy states in the symmetry sectors described by space-group characters χ_0^1 and χ_1^1 , GCNN ansätze for those states are taken to have the same architecture as for the ground state and the optimized ground state parameters are used as initial guess for the parameters of the ansätze. The ansätze therefore have the same number of layers and the same number of features in each layer as the ground state ansatz, however with different space group irreducible representation characters that reflect symmetry properties of a particular low-lying energy state. The ansätze can in general also have different spin parity P_{Z_2} equal to 1 (for χ_0^1 symmetry sector) or -1 (for χ_1^1 symmetry sector). Within this approach initial guess for a particular low-lying energy state wave function already has low variational energy and typical correlations characteristic for the low-energy eigenstates resulting in more stable training yielding more accurate results for the energy eigenvalues.

Within the VMC algorithm the quantum expectation value of any operator \hat{A}

$$\langle \hat{A} \rangle = \frac{\langle \psi | \hat{A} | \psi \rangle}{\langle \psi | \psi \rangle} \quad (27)$$

can be efficiently evaluated by rewriting the expectation value as a Monte Carlo average

$$\langle \hat{A} \rangle = \sum_{\vec{\sigma}} P(\vec{\sigma}) A^{loc}(\vec{\sigma}) \approx \frac{1}{N_s} \sum_{\vec{\sigma}} A^{loc}(\vec{\sigma}) \quad (28)$$

D(6)	e	R ³	R	R τ
χ_0	1	1	1	1
χ_1	1	1	-1	-1
χ_2	1	-1	1	-1
χ_3	1	-1	-1	1

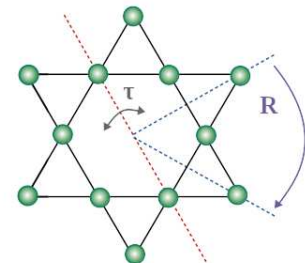


FIG. 7: Group elements of the little group for the crystal momentum $\vec{q} = (\pi, \pi/\sqrt{3})$ (M high symmetry point in the kagome lattice Brillouin zone) and corresponding irreducible representation characters. Here R is (anticlockwise) $\pi/3$ rotation around the center of the hexagonal plaquette and τ is reflection about the reflection line with angle $-\pi/3$ with respect to the x -axis.

with respect to the quantum probability distribution

$$P(\vec{\sigma}) = \frac{|\langle \vec{\sigma} | \psi \rangle|^2}{\langle \psi | \psi \rangle} \quad (29)$$

and estimating the average from N_s samples obtained using Markov chain Monte Carlo (MCMC) sampling methods that generate a sequence of N_s samples that asymptotically follow distribution $P(\vec{\sigma})$, where the local estimator $A^{loc}(\vec{\sigma})$ is

$$A^{loc}(\vec{\sigma}) = \frac{\langle \vec{\sigma} | \hat{A} | \psi \rangle}{\langle \vec{\sigma} | \psi \rangle} = \sum_{\vec{\sigma}'} \frac{\psi(\vec{\sigma}')}{\psi(\vec{\sigma})} \langle \vec{\sigma} | \hat{A} | \vec{\sigma}' \rangle. \quad (30)$$

Starting from the set of kernels within all layers initialized with Lecun normal initializer that draws samples from a truncated normal distribution centered on zero that gives correct variance of the output,¹³⁰ initial parameter values are updated within the SR algorithm at each iteration according to Eq. (17) with the free energy loss function described by Eq. (22) and the QGT regularization as in Eq. (18). The QGT and the free energy loss function gradient can also be efficiently evaluated as Monte Carlo averages. Whilst the free energy loss in Eq. (22) can not be efficiently evaluated from the MCMC samples since our calculations are performed with unnormalized neural-network ansatz wavefunctions and the entropy in Eq. (23) therefore can not be calculated, the loss function gradient within the VMC scheme can be evaluated from

$$\begin{aligned} \vec{\nabla}_{\vec{\alpha}} S &= - \sum_{\vec{\sigma}} P(\vec{\sigma}, \vec{\alpha}) \ln p(\vec{\sigma}, \vec{\alpha}) [\vec{\nabla}_{\vec{\alpha}} \ln p(\vec{\sigma}, \vec{\alpha}) \\ &\quad - \sum_{\vec{\sigma}'} P(\vec{\sigma}', \vec{\alpha}) \vec{\nabla}_{\vec{\alpha}} \ln p(\vec{\sigma}', \vec{\alpha})] \\ &\approx - \frac{1}{N_s} \sum_{\vec{\sigma}} \ln p(\vec{\sigma}, \vec{\alpha}) [\vec{\nabla}_{\vec{\alpha}} \ln p(\vec{\sigma}, \vec{\alpha}) \\ &\quad - \frac{1}{N_s} \sum_{\vec{\sigma}'} \vec{\nabla}_{\vec{\alpha}} \ln p(\vec{\sigma}', \vec{\alpha})], \end{aligned} \quad (31)$$

where $P(\vec{\sigma}, \vec{\alpha})$ is the probability distribution (29), $p(\vec{\sigma}, \vec{\alpha}) = |\psi(\vec{\sigma}, \vec{\alpha})|^2$, $\log p = 2\text{Re} \ln \psi$ and

$$\vec{\nabla}_{\vec{\alpha}} E = 2\text{Re}[\vec{f}] \quad (32)$$

with \vec{f} being

$$\begin{aligned} \vec{f} &= \sum_{\vec{\sigma}} P(\vec{\sigma}, \vec{\alpha}) \vec{O}^*(\vec{\sigma}) [E^{loc}(\vec{\sigma}) \\ &\quad - \sum_{\vec{\sigma}'} P(\vec{\sigma}', \vec{\alpha}) E^{loc}(\vec{\sigma}')] \\ &\approx \frac{1}{N_s} \sum_{\vec{\sigma}} \vec{O}^*(\vec{\sigma}) [E^{loc}(\vec{\sigma}) - \frac{1}{N_s} \sum_{\vec{\sigma}'} E^{loc}(\vec{\sigma}')] \end{aligned} \quad (33)$$

and $\vec{O} = \vec{\nabla}_{\vec{\alpha}} \ln \psi(\vec{\sigma}, \vec{\alpha})$ the gradient of log-amplitudes. We note that Eq. (32) is valid for non-holomorphic mapping $\vec{\alpha} \rightarrow \psi(\vec{\sigma}, \vec{\alpha})$ where $\text{Re}[\alpha_i]$ and $\text{Im}[\alpha_i]$ can be treated

as two independent real parameters and Eq. (32) can be applied to each separately.

Within the optimization procedure we take relatively large learning rate (imaginary time step) $\Delta\tau = 0.05$ in Eq.(17) and $N_s = 2^{12}$ or 2^{13} Monte Carlo samples in each training step for the clusters with 48 and 108 lattice sites respectively. The number of samples is taken to be the maximum number allowed by the available GPU memory restrictions since training with more samples helps the GCNN ansatz to learn the wave function representations that have better generalization properties to the parts of the Hilbert space that were not sampled. Although larger learning rates can cause non-monotonic behavior of the loss function and evaluated energy values as the training proceeds it helps the algorithm to escape from local minima and leads to higher accuracy for the final results despite temporary worsening of the algorithm performance during the optimization procedure.

We also find larger sensitivity of the algorithm to the choice of the QGT regularization parameters ϵ_1 and ϵ_2 in Eq.(21) than found in GCNN studies of J_1 - J_2 Heisenberg models on the square and triangular lattices.⁸¹ In our calculations ϵ_1 and ϵ_2 values are taken to be $\epsilon_1 = 0.001$ and $\epsilon_2 = 0.001$. We note that taking larger values of the regularization parameter can cause decrease of the obtained results accuracy which is related to the loss function symmetry breaking due to a weak regularizer. When a loss function is invariant under a continuous symmetry it has a manifold of equivalent degenerate minima. Any of these minima is then a valid solution to the optimiza-

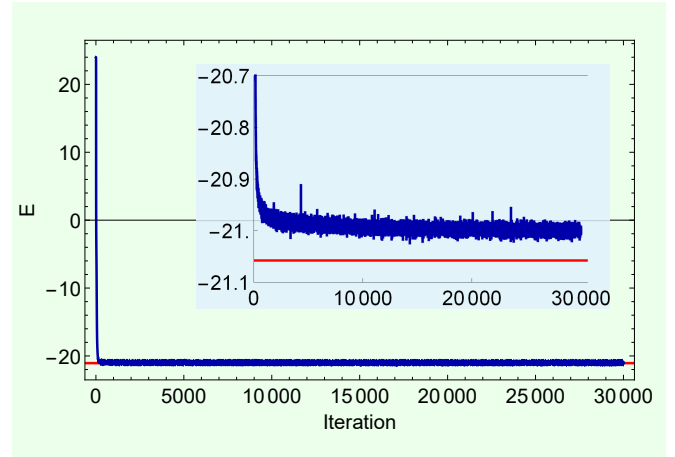


FIG. 8: The ground state energy obtained with SR minimization of the free energy loss defined in Eq. (22) for the system size of 48 lattice sites ($4 \times 4 \times 3$ cluster) and with periodic boundary conditions. The ground state GCNN ansatz with 6 layers and 6 features in each layer is fully symmetric with all discrete space-group symmetry characters $\chi_g = 1$ and has the spin parity $P_{Z_2} = 1$. The ansatz is therefore characterized by the crystal momentum $\vec{q} = (0, 0)$ (Γ high symmetry point in FIG. 4) and fully symmetric with respect to all dihedral group $D(6)$ point group transformations. The red line denotes ED result.¹⁰

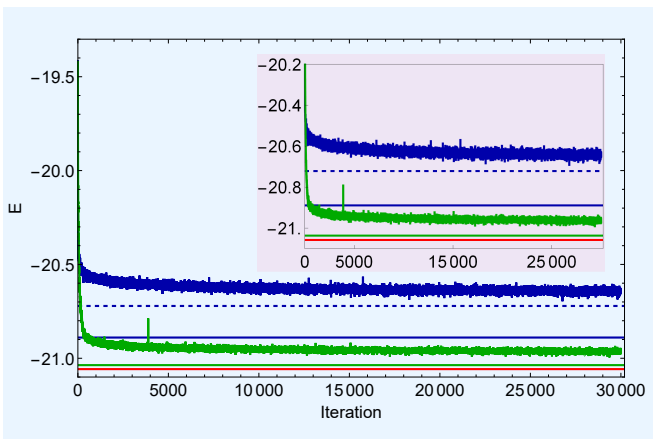


FIG. 9: The lowest energy eigenstates for the kagome lattice cluster with 48 sites ($4 \times 4 \times 3$ cluster) and periodic boundary conditions found in the symmetry sectors with space-group characters χ_0^1 (green line, $P_{\mathbb{Z}_2} = 1$) and χ_1^0 (blue line, $P_{\mathbb{Z}_2} = -1$). The eigenstates correspond to the first higher energy states above the ground state in the total $S = 0$ sector (χ_0^1) and the lowest energy state in the total $S = 1$ sector (χ_1^0). The energies are obtained with SR minimization of the energy loss function (19) and with help of the transfer learning scheme described in the main text. The GCNN ansätze for the eigenstates have 6 layers and 6 features in each layer equivalent to the GCNN architecture for the ground state shown in FIG. 8. For the energy eigenstate with space-group characters χ_0^1 the SR algorithm supplemented with transfer learning (initial parameters from the lowest energy eigenstate in the total $S = 0$ sector shown in FIG. 8) finds a local minimum corresponding to two triplons ($S = 1$ excitations) forming a total $S = 0$ eigenstate (dashed blue line). This finding reflects spinon Cooper pairing instability explained further in the main text. The red line denotes ED result.¹⁰

tion problem. The minima degeneracy is however lifted by introducing a small symmetry breaking term like a weak regularizer and the model then prefers one minimum over all other minima. Symmetries can be broken either explicitly due to an additional regularization term or spontaneously by couplings between the model parameters resulting in a slow convergence after initial fast decrease of the loss function value.¹⁵¹

The energy $E = \langle \psi | H | \psi \rangle / \langle \psi | \psi \rangle$ obtained for 48 lattice sites ($4 \times 4 \times 3$ cluster) with periodic boundary conditions at each training step with the free energy loss (22) and fully symmetric GCNN ansatz (space-group characters χ_0^0) is shown in FIG. 8. Converged energy value obtained with the SR imaginary time evolution corresponds to the ground state energy and the red line in FIG. 8 shows ED result.¹⁰ FIG. 8 demonstrates that GCNN approach with the ansatz composed of only 6 layers and with 6 features in each layer already allows the ground state energy accuracy with the relative error R of order 10^{-3} with respect to the ED result ($R = (E_{\chi_0^0}^{GCNN} - E_{\chi_0^0}^{ED}) / E_{\chi_0^0}^{ED} \approx 0.3\%$ with $E_{\chi_0^0}^{ED} = -21.057787063$ and $E_{\chi_0^0}^{GCNN} = -21.00 \pm 0.01$).

The lowest energy eigenstates in the symmetry sectors with space-group characters χ_0^1 and χ_1^0 , corresponding to the symmetry sectors of the first higher energy state above the ground state in the total $S = 0$ sector (χ_0^1) and the lowest energy state in the total $S = 1$ sector (χ_1^0) are further found with SR minimization of the energy loss function (19) and with help of the transfer learning scheme. Within the scheme the GCNN ansätze for the eigenstates are taken to have the same architecture (the same number of layers and the same number of features in each layer) as for the fully symmetric state with space-group characters χ_0^0 , however with different space group irreducible representation characters that reflect symmetry properties of a particular low-lying energy state. Also, whilst the eigenstate with space-group characters χ_0^1 has spin parity $P_{\mathbb{Z}_2} = 1$, the spin parity of the eigenstate with space-group characters χ_1^0 is $P_{\mathbb{Z}_2} = -1$. The approach helps to stabilize and expedite training within the SR optimization and to obtain more accurate results for the energy eigenvalues.

Converged energy eigenvalues in symmetry sectors χ_0^1 and χ_1^0 for 48 lattice sites cluster are shown in FIG. 9. As for the ground state (FIG. 8) the results for χ_0^1 clearly

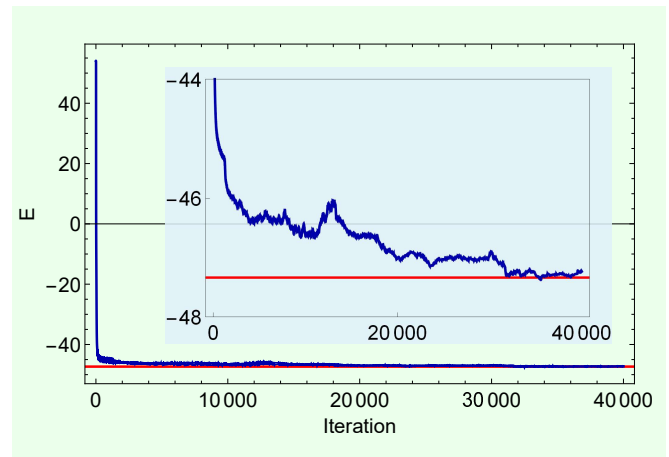


FIG. 10: The lowest energy eigenstate found in the symmetry sector with space-group characters χ_0^0 for the kagome lattice cluster with 108 lattice sites ($6 \times 6 \times 3$ cluster) and periodic boundary conditions. The energies are obtained with SR minimization of the free energy loss defined in Eq. (22) with a fully symmetric GCNN ansatz (with all space-group symmetry characters $\chi_g = 1$) having 4 layers and 4 features in each layer, the crystal momentum $\vec{q} = (0, 0)$ (Γ high symmetry point in FIG. 4) and parity $P_{\mathbb{Z}_2} = 1$. The red line denotes SU(2) symmetric DMRG result for the ground state energy.¹⁵ Converged energy value obtained with SR minimization, $E_{\chi_0^0} = -47.29(3)$, approaches the ground state energy value found by DMRG calculations ($E_0^{DMRG} = -47.33964$). However, the found eigenstate is not the ground state for $6 \times 6 \times 3$ cluster. Contrary to the result for 48 lattice sites cluster, for larger 108 lattice sites cluster the ground state has nonzero crystal momentum as explained further in the main text.

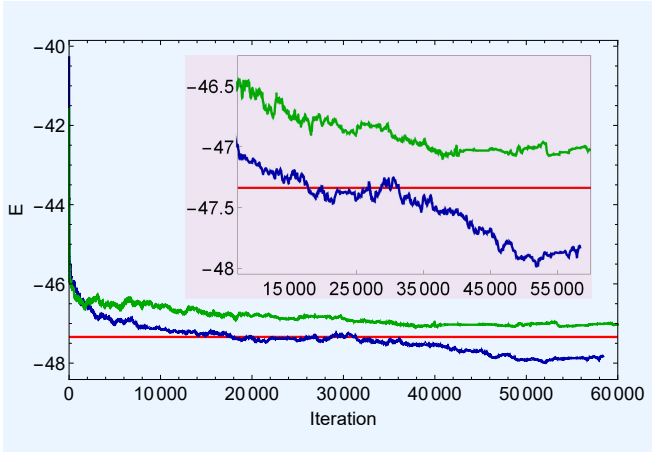


FIG. 11: The lowest energy eigenstates for the kagome lattice cluster with 108 sites ($6 \times 6 \times 3$ cluster) and periodic boundary conditions found in the symmetry sectors with space-group characters χ_0^1 (green line, $P_{Z_2} = 1$) and χ_1^0 (blue line, $P_{Z_2} = -1$). Both eigenstates are in the total $S = 0$ sector. The state with characters χ_0^1 has zero crystal momentum whilst the state with characters χ_1^0 has crystal momentum corresponding to the M high symmetry point in FIG. 4. The red line denotes SU(2) symmetric DMRG result for the ground state energy.¹⁵ Here the GCNN ansätze for the eigenstates have 4 layers and 4 features in each layer equivalent to the GCNN architecture for the lowest energy eigenstate in χ_0^0 symmetry sector shown in FIG. 10. The energies are obtained with SR minimization of the energy loss function (19) and with help of the transfer learning scheme described in the main text. Converged energy values obtained with SR minimization are $E_{\chi_0^1} = -47.01(7)$ and $E_{\chi_1^0} = -47.85(5)$. The lowest energy state for χ_1^0 symmetry sector has significantly lower energy than the ground state energy obtained with SU(2) symmetric DMRG calculations ($E_0^{DMRG} = -47.33964$). Further GCNN and VMC calculations for the lowest energy states in other symmetry sectors with crystal momentum corresponding to the M high symmetry point (FIG. 7) find a state with even lower energy that corresponds to the ground state for 108 sites cluster as explained further in the main text.

demonstrate ability of the algorithm to escape local minima and slow convergence due to a weak breaking of the continuous SU(2) symmetry. Obtained value of the singlet energy gap $\Delta_s^{GCNN} = 0.03 \pm 0.01$ is in good agreement with the ED result $\Delta_s^{ED} = 0.021217$. For the χ_0^1 sector containing the lowest energy eigenstate with the total $S = 1$ the algorithm however finds a low energy local minimum corresponding to a total $S = 0$ eigenstate with two triplon ($S = 1$) excitations forming a singlet. The nature of the found local minima can be seen by calculating the energy gap $\Delta = E_{\chi_0^1}^{GCNN} - E_{\chi_0^0}^{GCNN} \approx 0.36 \pm 0.01$ which is approximately twice the triplet energy gap obtained by ED calculations $\Delta_t^{ED} = 0.168217$. Δ_t^{GCNN} value however has 4–10% higher value than Δ_t^{ED} which reflects either a more complicated sign structure of the higher energy states or presence of a weak repulsive interaction between the quasiparticles. Starting from the

random coefficients for the GCNN ansatz in the χ_1^0 symmetry sector the SR algorithm either becomes unstable or finds a local minimum with significantly higher energy. Alternatively, if the ansatz coefficients are initialized with the parameters of the optimized χ_0^0 symmetry sector ansatz corresponding to a total $S = 0$ state the SR algorithm finds a local minimum that corresponds to the lowest total $S = 0$ energy eigenstate in the χ_1^0 symmetry sector and not to the lowest total $S = 1$ eigenstate. As it will be demonstrated further, presence of such strong local minimum reflects instability towards spinon Cooper pair creation in the same symmetry sector for larger system sizes where described eigenstate becomes global minimum within χ_1^0 symmetry sector.

We further repeat the same procedure to find low-lying energy states for the kagome lattice cluster with 108 lattice sites ($6 \times 6 \times 3$ cluster) and periodic boundary conditions. Since increased number of symmetries for larger system sizes results in more GCNN parameters for $6 \times 6 \times 3$ cluster, GCNN ansätze with only 4 layers and 4 features in each layer already yield to very accurate results. The SR minimization result for the χ_0^0 symmetry sector obtained with a fully symmetric GCNN ansatz is shown in FIG. 10 and the results for χ_0^0 and χ_1^0 symmetry sectors in FIG. 11. The red line in FIG. 10 and FIG. 11 denotes SU(2) symmetric DMRG result for the ground

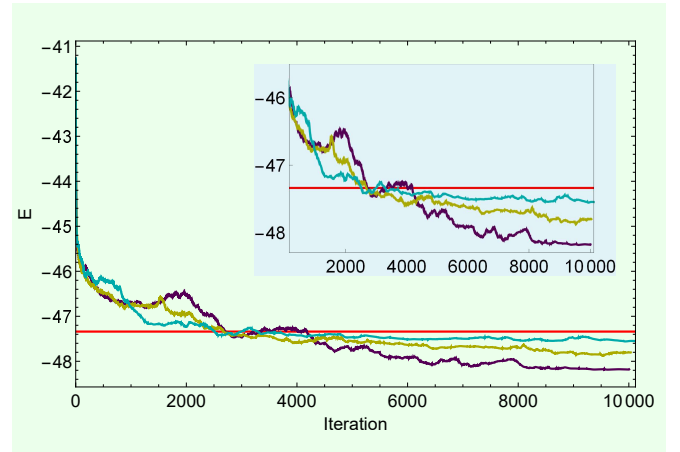


FIG. 12: Low-lying energy states for the kagome lattice cluster with 108 lattice sites ($6 \times 6 \times 3$ cluster) and with periodic boundary conditions in the symmetry sector characterized by crystal momentum $\vec{q} = (\pi, \pi/\sqrt{3})$ (M high symmetry point) and little group characters χ_0 , χ_1 and χ_3 in FIG. 7 (purple, yellow and cyan lines, respectively). The red line denotes SU(2) symmetric DMRG result for the ground state energy.¹⁵ Here GCNN ansätze have 4 layers and 4 features in each layer and parity $P_{Z_2} = -1$. The energies are obtained with SR minimization of the energy loss function (19) and with help of the transfer learning scheme described in the main text. Found energies are $E_{\chi_0} = -48.18(0)$, $E_{\chi_1} = -47.81(8)$ and $E_{\chi_3} = -47.54(4)$. For χ_2 characters in FIG. 7 found energy value is $E_{\chi_2} = -47.85(5)$ as shown in FIG. 11. For all eigenstates $\langle \vec{S}^2 \rangle \approx 0$.

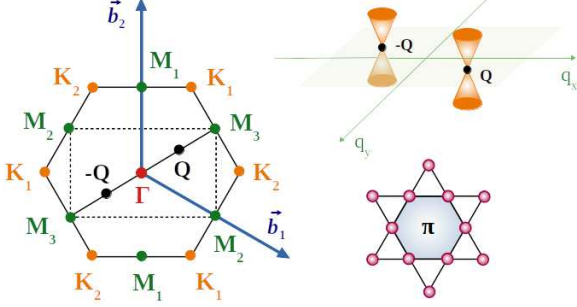


FIG. 13: Two Dirac nodes of the Dirac spin liquid (U(1) SL-[$0, \pi$] state), denoted here by $\pm\vec{Q}$. Magnetic Brillouin zone of the Dirac spin liquid is halved (dashed lines) since it is a π -flux ansatz with zero flux through the triangles and π -flux through the hexagons of the kagome lattice.

state energy.¹⁵ As it can be seen from FIG. 11 the lowest energy state for χ_1^0 symmetry sector already has significantly lower energy, $E_{\chi_1^0} = -47.85(5)$, than the ground state energy obtained with SU(2) symmetric DMRG calculations ($E_0^{DMRG} = -47.33964$).¹⁵ Using again transfer learning approach, we have further checked if any of the lowest energy states in other symmetry sectors for the crystal momentum corresponding to the M high symmetry point (symmetry sectors shown in FIG. 7) have even lower energy. Within this transfer learning step the optimization starts with coefficients of the optimized χ_1^0 ansatz for the neural networks with various characters corresponding to other symmetry sectors in FIG. 7 and parity $P_{\mathbb{Z}_2} = \pm 1$. Our calculations found the lowest energy for the eigenstate with characters χ_0 in FIG. 7 with parity $P_{\mathbb{Z}_2} = -1$ and $\vec{q} = (\pi, \pi/\sqrt{3})$. The results of the SR optimization for other symmetry sectors at the crystal momentum $\vec{q} = (\pi, \pi/\sqrt{3})$ and for eigenstates with parity $P_{\mathbb{Z}_2} = -1$ are shown in FIG. 12. The obtained ground state energy $E_0 = -48.18(0)$ is $\approx 1.78\%$ lower than the ground state energy obtained with DMRG calculations. We have also verified that the eigenstates for other crystal momenta and $P = -1$ have higher energy values than the eigenstates obtained for the crystal momentum corresponding to M high symmetry point which confirms that the spinon Cooper pairs have center of mass momentum $\vec{q} = (\pi, \pi/\sqrt{3})$. Also, the results clearly demonstrate change of the symmetry sector where the ground state is found that appears due to spinon Cooper pairing instability close to the spinon Fermi surface, here being two Dirac points. The observed instability has previously been predicted as one of the possible instabilities of the "parent" U(1) Dirac spin liquid.¹⁵² The instability is marginally relevant and it can be readily explained within fermionic parton theory.^{153–155}

Before proceeding to explanation of the found state we briefly comment on accuracy of the obtained results, quality of the obtained wavefunctions and sam-

pling scheme for both cluster sizes. In general for the systems with large number of possible competing many-body states, as it is the case for kagome lattice antiferromagnet, even small relative errors of order 10^{-3} in variational energy may result in the optimized ansatz wavefunction with correlations significantly different from the correlations of the true ground state. Presence of large number of the competing ground states is reflected in large number of low-lying total spin $S = 0$ singlet excitations below the first total spin $S = 1$ triplet excitation in the energy spectrum obtained in ED calculations for small lattice sizes¹⁰ that can host such possible competing states. A relative error of order 10^{-3} corresponds to several times singlet energy gap for smaller system sizes.¹⁰ However, within GCNN approach the low-lying singlet states correspond to different space-group irreducible representations with different space group characters χ_g and a small relative error for a chosen irreducible representation reflects a small quantitative rather than qualitative error that would result in significantly different ground-state wavefunction correlations. We also point out that the ground state energies obtained within presented GCNN approach provide significantly more accurate results than approaches based on other neural network architectures^{36–38} reflecting importance of introducing symmetry equivariance in neural network architectures.

We also note that indication of the spinon Cooper pairing instability and change of the ground state symmetry sector for the larger cluster can already be seen from the sampling schemes that yield the best ground state energies. Whilst for the 48 sites cluster the best variational energy is obtained by the free energy minimization within the total $S^z = 0$ sector where the samples are generated by exchanging spins at two randomly chosen lattice sites, for the 108 sites cluster the best results are found by sampling within the whole Hilbert space with samples generated by flipping a spin at random lattice site. The ground state wave function quality can be estimated by evaluating $\langle \vec{S}^2 \rangle$ which ideally should be zero since the exact ground state wavefunction has SU(2) symmetry. For the 108 sites cluster we find $\langle \vec{S}^2 \rangle \approx 2.5 \times 10^{-7}$ confirming very high quality of the obtained ground state wave function. For the 48 sites cluster we however find somewhat larger value of $\langle \vec{S}^2 \rangle \approx 0.14$. The obtained value still

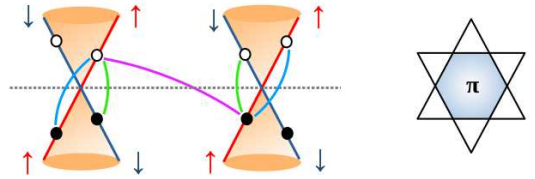


FIG. 14: The lowest energy inter-valley and intra-valley particle-hole excitations in the vicinity of the Dirac points.

indicates good quality of the obtained ground state wave function with only weakly broken SU(2) symmetry.⁸⁰ We also note that minimization within the whole Hilbert space for the 48 sites cluster, with samples generated by flipping a spin at random lattice site, yields better result for \bar{S}^2 ($\approx 10^{-7}$) and less accurate result for the ground state energy. Moreover, such minimization requires larger number of samples, exhibits slower convergence and finds significantly higher energy values for the low-lying energy states with more complicated sign structures than the energies found by minimization within the total $S^z = 0$ sector that are shown in FIG. 9.

In the Schwinger fermion parton construction a spin-1/2 operator at site i is represented by fermionic spinons $f_{i\alpha}$ with $\alpha \in \uparrow, \downarrow$:

$$\vec{S}_i = \frac{1}{2} f_{i\alpha}^\dagger \vec{\sigma}_{\alpha\beta} f_{i\beta}, \quad (34)$$

where $\sigma = (\sigma^x, \sigma^y, \sigma^z)$ are Pauli matrices. Within mean-field theory symmetric spin liquids are obtained by introducing mean-field parameters χ_{ij} and Δ_{ij} :

$$\begin{aligned} \chi_{ij} \delta_{\alpha\beta} &= 2 \langle f_{i\alpha}^\dagger f_{j\beta} \rangle, \\ \Delta_{ij} \epsilon_{\alpha\beta} &= -2 \langle f_{i\alpha} f_{j\beta} \rangle, \end{aligned} \quad (35)$$

where $\delta_{\alpha\beta}$ is Kronecker delta and $\epsilon_{\alpha,\beta}$ is the completely antisymmetric tensor. Since the parton construction enlarges the Hilbert space of the original spin model, the physical spin state is obtained by introducing constraint of one spinon per site:

$$\begin{aligned} f_{i\alpha}^\dagger f_{i\alpha} &= 1, \\ f_{i\alpha} f_{i\beta} \epsilon_{\alpha\beta} &= 0, \end{aligned} \quad (36)$$

where repeated indices are summed over. Within the parton theory the magnetic excitations then correspond to deconfined spinons and non-magnetic (total spin $S = 0$) excitations to fluxes (or vortices) of the Z_2 gauge field called visons.

Projective symmetry group (PSG) calculations with fermionic partons find both gapped and gapless symmetry allowed Z_2 spin liquid states.^{154,155} These spin liquid states are continuously connected to different parent $U(1)$ gapless spin liquid states that in general have the following mean-field ansatz

$$H_{U(1)SL} = \chi \sum_{\langle ij \rangle} \nu_{ij} (f_{i\alpha}^\dagger f_{j\alpha} + h.c.), \quad (37)$$

where $\chi \in \mathbb{R}$ and $\nu_{ij} = \pm 1$ characterizes signs of nearest-neighboring hopping terms. Different $U(1)$ spin liquids then correspond to different spinon hopping phases around hexagonal and triangular plaquettes of the kagome lattice. VMC calculations showed that the $U(1)$ Dirac spin liquid state with zero-flux through the triangles and π -flux through the hexagons ($U(1)$ SL-[0, π] state) has considerably lower energy compared to many other competing states.^{20,28,31,35,52,53,156–158} VMC calculations have also shown that all gapped and gapless Z_2

spin liquids are higher in energy compared to the parent $U(1)$ gapless spin liquids those Z_2 spin liquids are continuously connected to.³¹ The magnetic Brillouin zone and positions of two Dirac nodes of the $U(1)$ Dirac state are illustrated in FIG. 13. Such state in two-dimensions has an emergent SU(4) symmetry.

Within fermionic parton theory spin triplet (total $S = 1$) excitations correspond to the particle-hole excitations near Dirac points since a spin flip with momentum $\vec{q}_1 - \vec{q}_2$ can be written as $S^+(\vec{q}_1 - \vec{q}_2) = f_{\uparrow}^\dagger(\vec{q}_1) f_{\downarrow}(\vec{q}_2)$. The lowest energy inter-valley and intra-valley particle-hole excitations are illustrated in FIG. 14. DMRG calculations of the transfer matrix spectrum in the $S^z = 1$ sector²⁰ found Dirac cone structure for the particle-hole mode denoted by magenta line in FIG. 14 indicating presence of Dirac points in the spectrum of the kagome lattice antiferromagnetic Heisenberg model. Also, for the gapless Z_2 spin liquid states found within PSG approach^{154,155} Dirac nodes in the spinon spectrum are protected by symmetry. Our results however show that for the highly symmetric $6 \times 6 \times 3$ cluster that contains all three high symmetry points in the Brillouin zone (Γ , M and K points in FIG. 4) the ground state has finite crystal momentum. We further argue that the found state is a spinon-pair density wave (PDW) state that does not break time-reversal symmetry nor any of the lattice symmetries. This is supported by the results for chiral order parameter and spin and dimer structure factors presented further in this section.

PDW state is a state in which Cooper pairs (in this case spinon Cooper pairs) have finite center of mass momentum. The first found example of PDW state is the Fulde-Ferrell-Larkin-Ovchinnikov (FFLO) state^{159,160} which appears in superconductors in the presence of a Zeeman magnetic field and breaks time-reversal symmetry. It was subsequently conjectured that for systems with strong interactions a PDW could occur without time-reversal symmetry breaking and was studied in the context of underdoped cuprate superconductors in connection with pseudogap phase.^{121–125} For such PDW state the spatial average of the superconducting order vanishes which allows the state to be distinguished from the coexisting charge density wave and superconducting order.

In a PDW state the mean-field parameter that represents Cooper pairs

$$\Delta_{\sigma,\sigma'}^*(\vec{r}_i, \vec{r}_j) \equiv \langle f_{\sigma}^\dagger(\vec{r}_i) f_{\sigma'}(\vec{r}_j) \rangle \quad (38)$$

is not translation invariant, that is $\Delta^*(\vec{r}_i, \vec{r}_j) \neq \Delta^*(\vec{r}_i + \vec{R}, \vec{r}_j + \vec{R})$, where \vec{R} is any Bravais lattice vector. In the context of spin liquids that would mean that $\Delta_{\sigma,\sigma'}^*(\vec{r}_i, \vec{r}_j)$ is not invariant with respect to combined lattice translation and gauge group transformations within the PSG approach. Symmetries of the translation invariant states can be classified by the point group irreducible representations (for example s-wave, d-wave or p-wave states), properties under spin rotations in the absence of spin-orbit coupling (singlet or triplet states), and according

to behavior with respect to time reversal where in general the state can be time-reversal symmetric or break the symmetry (for example $p_x + ip_y$ state). For spinons corresponding states are Z_2 spin liquids obtained within PSG approach.

Contrary to translation invariant states, a PDW state exhibits spatial modulation, that has nontrivial dependence on \vec{R} . Whilst $\Delta^*(\vec{r}_i, \vec{r}_j)$ is nonzero for a PDW, its spatial average

$$\Delta_{\sigma, \sigma'}^{*(0)}(\vec{r}_i, \vec{r}_j) = \frac{1}{N_{u.c.}} \sum_{\vec{R}} \Delta_{\sigma, \sigma'}^*(\vec{r}_i + \vec{R}, \vec{r}_j + \vec{R}) = 0 \quad (39)$$

where $N_{u.c.}$ is the number of unit cells, and a PDW state is characterized by the smallest value of the wavevector \vec{P} for which

$$\Delta_{\sigma, \sigma'}^{*(\vec{P})}(\vec{r}_i, \vec{r}_j) = \frac{1}{N_{u.c.}} \sum_{\vec{R}} e^{i\vec{P}\vec{R}} \Delta_{\sigma, \sigma'}^*(\vec{r}_i + \vec{R}, \vec{r}_j + \vec{R}) \quad (40)$$

has non-zero value. Similar average will then also be nonzero at wavevectors $n\vec{P}$.

If Cooper pairs are formed between fermions (spinons) with momenta $\vec{Q} - \vec{k}$ and $\vec{Q} + \vec{k}$ near point \vec{Q} on the Fermi surface the pairs carry momenta $\vec{P} = 2\vec{Q}$. Once such pairing occurs $U(1)$ gauge group is reduced to Z_2 . Similarly as for the nodal Z_2 spin liquids that can be obtained within PSG (of which Kitaev spin liquid is a known example¹⁶¹) where lines of gap nodes intersect with Fermi surface causing a number of gapless Dirac-like nodal points in the spinon spectrum, the Fermi surface for a PDW can not be fully gapped since the gap parameter changes sign when translated for 1/2 of the PDW period. The Dirac-like nodal points for nodal spin liquids are known to be perturbatively stable as long as time-reversal symmetry is not broken.¹⁶² Equivalently gapless Fermi surface is stable since $U(1)$ gauge field was reduced to Z_2 which is gapped. We further point out that although a PDW in general breaks lattice translation symmetry, for the special case when PDW period is two lattice constants the lattice translation symmetry is not broken since translation for one lattice constant corresponds to a uniform gauge transformation. In that case PDW state can occur without breaking any lattice symmetries. In addition if the Cooper pairs with momenta \vec{P} and $-\vec{P}$ coexist corresponding two component mean-field parameter does not break time reversal symmetry¹⁶³ and has the form

$$\Delta_{\sigma, \sigma'}^*(\vec{r}_i, \vec{r}_j) = F(\vec{r} - \vec{r}') [\Delta_{\sigma, \sigma'}^{*(\vec{P})} \cdot e^{i\vec{P}\vec{R}} + \Delta_{\sigma, \sigma'}^{*(-\vec{P})} \cdot e^{-i\vec{P}\vec{R}}], \quad (41)$$

where $F(\vec{r} - \vec{r}')$ is a short-range function (for example d-wave like) and $\vec{R} = (\vec{r}_1 + \vec{r}_2)/2$.

For the ground state found for the 108 lattice sites kagome cluster Fermi surface corresponds to two Dirac nodes illustrated in FIG. 13 and spinon Cooper pairs are formed from spinons with momenta $\pm\vec{Q} - \vec{k}$ and $\pm\vec{Q} + \vec{k}$

resulting in a PDW with $\vec{P} = 2\vec{Q} = (\vec{b}_1 + \vec{b}_2)/2$ with \vec{b}_1 and \vec{b}_2 being two primitive basis vectors in the reciprocal lattice (FIG. 4) and \vec{P} corresponding to the M high symmetry point in the Brillouin zone. Therefore the PDW has period of two lattice constants and does not break translation symmetry or any of the point group symmetries. The PDW mean-field parameter coupling to spinons can be described with

$$H_{\vec{P}}^{\sigma\sigma'} = \Delta_{\vec{P}}^{\sigma\sigma'} \sum_{\vec{k}} F(\vec{k}) f_{\sigma, \vec{k} + \frac{\vec{P}}{2}}^\dagger f_{\sigma', -\vec{k} + \frac{\vec{P}}{2}}, \quad (42)$$

where $F(\vec{k})$ is an internal form factor that can be, for example, s -wave or d -wave or mixed. For the PDW with $\vec{P}/2 = \vec{Q}$ and d -form factor Dirac points in the spinon spectrum remains gapless. The gauge fluctuations are gapped due to reduction of $U(1)$ gauge group to Z_2 as it can be seen in FIG. 11 (the state represented by green line that corresponds to visons that are vortex-like excitations). Furthermore the points \vec{P} and $-\vec{P}$ are equivalent since they are connected by a reciprocal lattice vector and the state does not break time reversal symmetry which we confirmed by calculating the chiral order parameter¹⁹

$$\chi_i = \langle \vec{S}_{i_1} \cdot (\vec{S}_{i_2} \times \vec{S}_{i_3}) \rangle, \quad (43)$$

where i denotes triangular plaquettes of the kagome lattice ($i \in \Delta_i, \nabla_i$). The chiral order parameter vanishes for the ground states obtained for both, 108 and 48 lattice sites, clusters.

We further note that a PDW can in general induce secondary orders. Studying such induced orders has

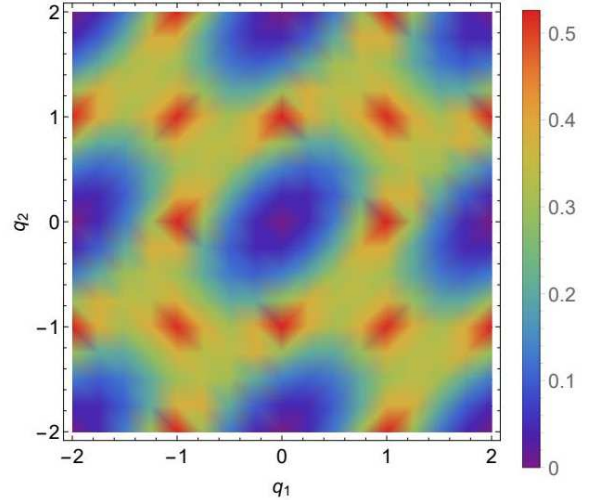


FIG. 15: The static spin structure factor $S_f^z(\vec{q})$ defined in Eq. (46) for the system size of 48 lattice sites ($4 \times 4 \times 3$ cluster) and with periodic boundary conditions calculated using optimized ground state GCNN ansatz. The structure factor is shown as a function of the wavevector $\vec{q} = (q_1, q_2)$ where components $q_1 = n_1/N_1$ and $q_2 = n_2/N_2$ are in units of the primitive basis vectors \vec{b}_1 and \vec{b}_2 shown in FIG. 4 and $N_1 = N_2 = 4$.

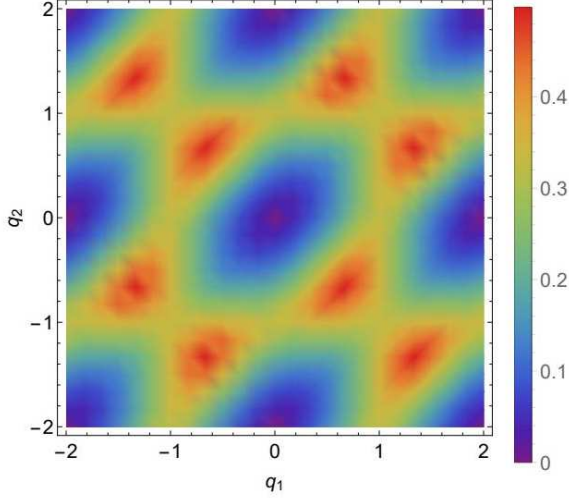


FIG. 16: The static spin structure factor $S_f^z(\vec{q})$ defined in Eq. (46) for the system size of 108 lattice sites ($6 \times 6 \times 3$ cluster) and with periodic boundary conditions calculated using optimized ground state GCNN ansatz. The structure factor is shown as a function of the wavevector $\vec{q} = (q_1, q_2)$ where components $q_1 = n_1/N_1$ and $q_2 = n_2/N_2$ are in units of the primitive basis vectors \vec{b}_1 and \vec{b}_2 shown in FIG. 4 and $N_1 = N_2 = 6$.

great importance in understanding relevance of PDW orders in cuprates,^{122,164–170} primarily charge density wave (CDW) orders and also Ising nematic, magnetization density wave (MDW) and translation invariant charge-4e superconducting orders. For the found ground state relevant possible induced order parameters are CDW, nematic and 4 spinon order parameters, where 4 spinon order parameter is equivalent to a charge-4e superconducting order parameter for electrons. If Cooper pairs form at momenta \vec{P} and $-\vec{P}$, CDW order appears as a second harmonic of the fundamental PDW order and has the form $\rho_{2\vec{P}} \propto \Delta_{\vec{P}} \Delta_{-\vec{P}}^*$ with ordering wavevector $\vec{K} = 2\vec{P}$ whilst nematic ordering has the form $N \propto |\Delta_{\vec{P}}|^2 + |\Delta_{-\vec{P}}|^2$. In general CDW order breaks lattice translation symmetry whilst nematic order breaks lattice rotation symmetry. However for the PDW period equal to two lattice constants, as it is the case for the kagome lattice PDW where \vec{P} corresponds to the M high symmetry point wavevector and \vec{P} and $-\vec{P}$ differ by a reciprocal lattice vector, lattice translation and rotation symmetries are not broken.

The 4 spinon order parameter is

$$\Delta^{*(4)}(i, j, k, l) \equiv \langle f_{\sigma_i}^\dagger(\vec{r}_i) f_{\sigma_j}^\dagger(\vec{r}_j) f_{\sigma_k}^\dagger(\vec{r}_k) f_{\sigma_l}^\dagger(\vec{r}_l) \rangle, \quad (44)$$

where $i \equiv (\vec{r}_i, \sigma_i)$. If $\Delta^{*\sigma, \sigma'}(\vec{r}, \vec{r}') \neq 0$ then also some components of the $\Delta^{*(4)}(i, j, k, l)$ order parameter will be nonzero, which can be seen by rewriting the order

parameter at the mean field level as

$$\begin{aligned} \Delta^{*(4)}(i, j, k, l) &\sim \Delta^*(i, j) \Delta^*(k, l) + \Delta^*(i, l) \Delta^*(j, k) \\ &\quad - \Delta^*(i, k) \Delta^*(j, l). \end{aligned} \quad (45)$$

Although the uniform component $\Delta^{*(0)}$ described by Eq. (39) vanishes, the uniform component of $\Delta^{*(4)}$ which is of the form $\Delta_{\vec{P}} \Delta_{-\vec{P}}$ does not vanish. Such ordering in some circumstances can be more robust than PDW ordering, as in cases when thermal or quantum fluctuations destroy PDW order however not charge-4e order^{171,172} whilst Fermi surface of gapless quasiparticles remains. In the context of spin liquids such state would be a Z_4 spin liquid with gapped gauge fluctuations and spinon Fermi surface.¹⁵² A Z_4 spin liquid cannot be described within a simple mean-field theory that is quadratic in terms of fermion operators. Also vortex-like excitations (visons) of the Z_4 gauge field carry $1/4$ of the flux quantum, and since a Z_4 vison is different from its time-reversed anti-vison with the flux $-1/4$ of the flux quantum, visons in a Z_4 spin liquid necessarily break time-reversal symmetry. We have found that all eigenstates found within our GCNN and VMC approach have vanishing chiral order parameter confirming time-reversal symmetry of the eigenstates and indicating presence of the spinon PDW ordering.

We have further calculated spin and dimer structure factors for the found ground states to find additional signatures of the gapless spinon spectrum and spinon pair

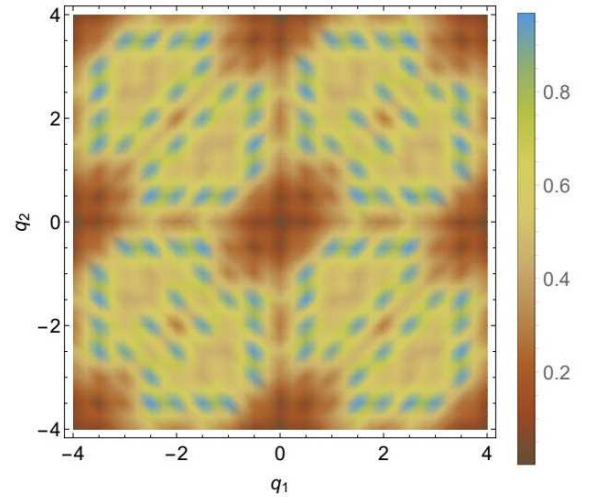


FIG. 17: Dimer structure factor $S_f^z(\vec{q})$ defined in Eq. (47) for the system size of 48 lattice sites ($4 \times 4 \times 3$ cluster) and with periodic boundary conditions calculated using optimized ground state GCNN ansatz. The structure factor is shown as a function of the wavevector $\vec{q} = (q_1, q_2)$ where components $q_1 = n_1/N_1$ and $q_2 = n_2/N_2$ are in units of the primitive basis vectors \vec{b}_1 and \vec{b}_2 shown in FIG. 4 and $N_1 = N_2 = 4$.

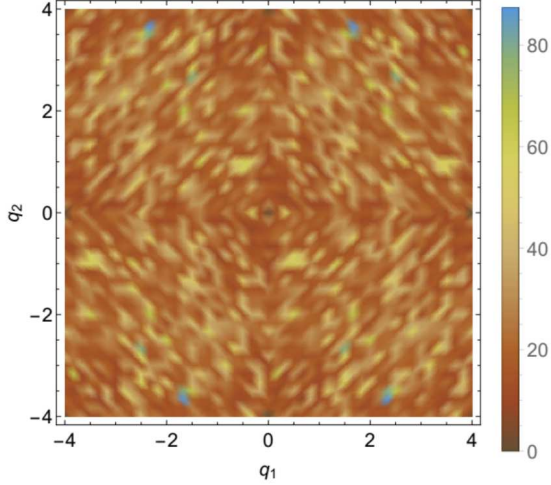


FIG. 18: Dimer structure factor $S_f^z(\vec{q})$ defined in Eq. (47) for the system size of 108 lattice sites ($6 \times 6 \times 3$ cluster) and with periodic boundary conditions calculated using optimized ground state GCNN ansatz. The structure factor is shown as a function of the wavevector $\vec{q} = (q_1, q_2)$ where components $q_1 = n_1/N_1$ and $q_2 = n_2/N_2$ are in units of the primitive basis vectors \vec{b}_1 and \vec{b}_2 shown in FIG. 4 and $N_1 = N_2 = 6$.

density wave order. The static spin structure factor

$$S_f^z(\vec{q}) = \frac{1}{N} \sum_{ij} e^{i\vec{q} \cdot (\vec{r}_i - \vec{r}_j)} \langle S_i^z S_j^z \rangle \quad (46)$$

is calculated using optimized ground state GCNN ansätze for both cluster sizes. We note that due to spin rotation symmetry $S_f^z(\vec{q}) = S_f(\vec{q})/3$ with $S_f(\vec{q}) = \sum_{i \in \{x, y, z\}} S_f^i(\vec{q})$ which also holds approximately when $SU(2)$ symmetry is only weakly broken. The wavevector $\vec{q} = (q_1, q_2)$ components $q_1 = n_1/N_1$ and $q_2 = n_2/N_2$ are in units of two primitive basis vectors \vec{b}_1 and \vec{b}_2 shown in FIG. 4 with $n_i = \{0, \dots, N_i - 1\}$ for $i \in 1, 2$ and $3 \times N_1 \times N_2 = N$ being the number of lattice sites. The results are shown in FIG. 15 and FIG. 16 for $N = 48$ and $N = 108$ sites clusters with periodic boundary conditions. We note that since the unit cell contains three atoms the structure factor is not invariant under reciprocal lattice vector shifts. To fully describe correlations between all spins we calculate the structure factor in the extended Brillouin zone with $0 \leq q_1 \leq 2$ and $0 \leq q_2 \leq 2$. At large $|\vec{q}|$ the spectral weight is concentrated around the edge of the extended Brillouin zone with broad response and not very sharp or pronounced maxima, corresponding to the results obtained with DMRG¹⁵ and projected fermionic wave-function⁵³ approaches. Whilst for the 48 sites cluster maxima are located at $(q_1, q_2) = (0, 1), (1, 0)$ and $(1, 1)$, for the 108 sites cluster maxima are found close to the M-points of the extended Brillouin zone and the structure factor has pinch-point like features that signal algebraically decaying spin-spin correlations in real space¹⁷³ and gapless

spinon spectrum.

Moreover results for the static spin structure factor clearly demonstrate that the ground state is a disordered state. Namely, maxima of the structure factor remain at approximately the same small value when the system size is increased (≈ 0.526 and ≈ 0.498 for 48 and 108 sites clusters, respectively) which is in sharp contrast to the behavior of the structure factor maxima for magnetic ordered systems. The quantity that describes how sharp is the structure factor peak is correlation ratio R ⁷⁶ defined as $R = 1 - S_f(\vec{q}_{max} + \delta\vec{q})/S_f(\vec{q}_{max})$ where \vec{q} is the peak momentum and $\vec{q}_{max} + \delta\vec{q}$ the neighboring momentum. For the magnetic ordered phase the structure factor maximum becomes sharper and approaches delta-function Bragg peak with the system size increase and corresponding correlation ratio R scales to one. For disordered phases however the structure factor maxima are broad and do not become sharper and higher with increasing system size and R in that case therefore scales to zero.

The spin structure factor however does not clearly indicate the nature of the disordered ground state state, since similar structure factor results are found for both \mathbb{Z}_2 and $U(1)$ Dirac spin liquid phases.^{15,53} It also does not provide information about possible valence bond crystal (VBC) phases. We therefore also calculate dimer structure factor

$$S_f^D(\vec{q}) = \frac{1}{N} \sum_{i,j,k,l} e^{i\vec{q} \cdot (\vec{r}_{ik} - \vec{r}_{jl})} D((i, k), (j, l)), \quad (47)$$

where $\vec{r}_{ab} = (\vec{r}_a + \vec{r}_b)/2$ denote midpoints on each bond and

$$D((i, k), (j, l)) = \langle \vec{S}_i \cdot \vec{S}_k \vec{S}_j \cdot \vec{S}_l \rangle - \langle \vec{S}_i \cdot \vec{S}_k \rangle \langle \vec{S}_j \cdot \vec{S}_l \rangle \quad (48)$$

is the connected dimer-dimer correlation function with k and l being the nearest neighboring sites of i and j . We also note that dimer-dimer correlators in Eq. (48) can be the most efficiently evaluated as covariance of the local estimators for $\vec{S}_i \cdot \vec{S}_k$ and $\vec{S}_j \cdot \vec{S}_l$. If we denote $\vec{S}_i \cdot \vec{S}_k$ by \hat{A} and $\vec{S}_j \cdot \vec{S}_l$ by \hat{B} the correlators in Eq.(48) can be evaluated as

$$\begin{aligned} \langle \hat{A} \hat{B} \rangle &= \frac{\langle \psi | \hat{A} \hat{B} | \psi \rangle}{\langle \psi | \psi \rangle} = \sum_{\vec{\sigma}} P(\vec{\sigma}) [A^{loc}(\vec{\sigma})]^* B^{loc}(\vec{\sigma}) \\ &\approx \frac{1}{N_s} \sum_{\vec{\sigma}} [A^{loc}(\vec{\sigma})]^* B^{loc}(\vec{\sigma}) \end{aligned} \quad (49)$$

where $P(\vec{\sigma})$ is the probability distribution in Eq. (29). The results for the dimer-dimer structure factor for 48 and 108 lattice sites clusters are shown in FIG. 17 and FIG. 18. For the 48 sites cluster the structure factor $S_f^D(\vec{q})$ does not have very sharp peaks. The results are similar to the results obtained for the same cluster with DMRG calculations¹³ with slightly higher maxima values (maximum value ≈ 0.933). However, contrary to the DMRG results, overall magnitude of the dimer structure factor significantly increases for the 108 sites cluster.

The structure factor exhibits numerous peaks, with several more pronounced peaks and its maximum value is ≈ 87.370 . This behavior reflects existence of the spinon PDW and the secondary order parameters induced by the spinon PDW. Since instability towards finite momentum Cooper pairs leads to PDW ground state only for larger system sizes, to further study scaling of the correlation ratio $R^D = 1 - S_f^D(\vec{q}_{max}^D + \delta\vec{q})/S_f^D(\vec{q}_{max}^D)$ and maximum of the dimer structure factor at the wavevector \vec{q}_{max}^D as functions of the system size further GCNN and VMC calculations for larger system sizes are necessary. This computationally very challenging task is beyond the scope of our current study and is one of our future research directions together with the formulation of an effective theory for the studied kagome system that can capture appearance of the PDW and all possible induced orders. An interesting question is also behavior of the system upon doping studied previously assuming U(1) Dirac spin liquid ground for undoped kagome system.¹⁷⁴

V. CONCLUSIONS

We have studied properties of the spin-1/2 kagome antiferromagnet using GCNN and VMC approach, an advanced recently developed machine learning technique that allows studying strongly frustrated models with high accuracy. Unlike many other neural network architectures that lack generalization quality for frustrated spin systems, GCNNs are deep neural network architectures equivariant with respect to all space group transformations that in addition to expressivity also possess greater generalization quality, that is ability to learn from a limited number of samples. This greater generalization quality allows efficient neural network training and more accurate solutions for the optimal network parameters. Since neural networks in general do not exhibit bias towards any particular kind of states, unlike density matrix

renormalization group and other variational methods including tensor network approaches, our study provides an important step in clarifying the kagome antiferromagnet properties and a reference to check validity of the results obtained with other methods.

Contrary to the results obtained with various other methods, that predicted Z_2 or U(1) Dirac spin liquid states, we have found that the ground state of the kagome lattice antiferromagnet is a spinon PDW that does not break time-reversal symmetry or any of the lattice symmetries. The found ground state has significantly lower energy than the lowest energy states found by the SU(2) symmetric density matrix renormalization group calculations and other methods. The PDW state appears due to the spinon Cooper pairing instability close to two Dirac points in the spinon energy spectrum resulting in formation of spinon Cooper pairs with finite center of mass momentum. Further examination of the found spinon Cooper pairing instability requires calculation of the system properties for larger system sizes. This computationally very challenging task is one of our future research directions together with formulation of an effective theory that would capture PDW formation on the kagome lattice and possible PDW induced secondary orders. Additional studies are also necessary to examine stability of such states to various perturbations, for example further neighbor couplings.

Acknowledgments

We thank Dhiman Bhowmick, Jon David Spalding, Kathyat Deepak Singh, Yasir Iqbal, Dario Poletti, Daniel Leykam, Wei Zhu and Shoushu Gong for helpful discussions. This work was supported by the National Research Foundation, Singapore under the NRF fellowship award (NRF-NRFF12-2020-005), and the Google cloud research credits academic research grant.

¹ R. Moessner, and A. P. Ramirez, *Physics Today* **59** (2), 24–29 (2006).
² C. Lhuillier, arXiv:cond-mat/0502464.
³ B. Schmidt, P. Thalmeier, *Physics Reports* **703**, 1-59 (2017).
⁴ L. Balents, *Nature* **464**, 199 - 208 (2010).
⁵ L. Savary, and L. Balents, *Rep. Prog. Phys.* **80**, 016502 (2017).
⁶ C. Broholm, R. J. Cava, S. A. Kivelson, D. G. Nocera, M. R. Norman, and T. Senthil, *Science* **367**, eaay0668 (2020).
⁷ Y. Zhou, K. Kanoda, and T.-K. Ng, *Rev. Mod. Phys.* **89**, 025003 (2017).
⁸ P. A. Lee, *Rep. Prog. Phys.* **71**, 012501 (2008).
⁹ G. Semeghini, H. Levine, A. Keesling, S. Ebadi, T. T. Wang, D. Bluvstein, R. Verresen, H. Pichler, M. Kalinowski, R. Samajdar, A. Omran, S. Sachdev, A. Vishwanath, M. Greiner, V. Vuletic, and M. D. Lukin, *Science* **374**, 1242 (2021).

¹⁰ A. M. Läuchli, J. Sudan, and R. Moessner, *Phys. Rev. B* **100**, 155142 (2019).
¹¹ A. Wietek, and A. M. Läuchli, *Phys. Rev. B* **102**, 020411(R) (2020).
¹² H. J. Changlani, D. Kochkov, K. Kumar, B. K. Clark, and E. Fradkin, *Phys. Rev. Lett.* **120**, 117202 (2018).
¹³ H. C. Jiang, Z. Y. Weng, and D. N. Sheng, *Phys. Rev. Lett.* **101**, 117203 (2008).
¹⁴ S. Yan, D. A. Huse, and S. R. White, *Science* **332**, 1173-1176 (2011).
¹⁵ S. Depenbrock, I. P. McCulloch, and U. Schollwöck, *Phys. Rev. Lett.* **109**, 067201 (2012).
¹⁶ H.-C. Jiang, Z. Wang, and L. Balents, *Nature Physics* **8**, 902-905 (2012).
¹⁷ S. Nishimoto, N. Shibata, and C. Hotta, *Nature Communications* **4**, 2287 (2013).
¹⁸ B. Bauer, L. Cincio, B. P. Keller, M. Dolfi, G. Vidal, S. Trebst, A. W. W. Ludwig, *Nature Communications* **5**,

- 5137 (2014).
- ¹⁹ S.-S. Gong, W. Zhu, and D. N. Sheng, *Scientific Reports* **4**, 6317 (2014).
- ²⁰ Y.-C. He, M. P. Zaletel, M. Oshikawa, and F. Pollmann, *Phys. Rev. X* **7**, 031020 (2017).
- ²¹ G. Evenbly, and G. Vidal, *Phys. Rev. Lett.* **104**, 187203 (2010).
- ²² Z. Y. Xie, J. Chen, J. F. Yu, X. Kong, B. Normand, T. Xiang, *Phys. Rev. X* **4**, 011025 (2014).
- ²³ J.-W. Mei, J.-Y. Chen, H. He, and X.-G. Wen, *Phys. Rev. B* **95**, 235107 (2017).
- ²⁴ S. Niu, J. Hasik, J.-Y. Chen, and D. Poilblanc, *Phys. Rev. B* **106**, 245119 (2022).
- ²⁵ H. J. Liao, Z. Y. Xie, J. Chen, Z. Y. Liu, H. D. Xie, R. Z. Huang, B. Normand, T. Xiang *Phys. Rev. Lett.* **118**, 137202 (2017).
- ²⁶ R. Haghshenas, S.-S. Gong, and D. N. Sheng, *Phys. Rev. B* **99**, 174423 (2019).
- ²⁷ S. Jiang, P. Kim, J. H. Han, and Y. Ran, *SciPost Phys.* **7**, 006 (2019).
- ²⁸ Y. Ran, M. Hermele, P. A. Lee, and X.-G. Wen, *Phys. Rev. Lett.* **98**, 117205 (2007).
- ²⁹ Y. Iqbal, F. Becca, and D. Poilblanc, *Phys. Rev. B* **83**, 100404(R) (2011).
- ³⁰ B. K. Clark, J. M. Kinder, E. Neuscamman, G. K.-L. Chan, and M. J. Lawler, *Phys. Rev. Lett.* **111**, 187205 (2013).
- ³¹ Y. Iqbal, F. Becca, and D. Poilblanc, *Phys. Rev. B* **84**, 020407(R) (2011).
- ³² T. Tay, and O. I. Motrunich, *Phys. Rev. B* **84**, 020404(R) (2011).
- ³³ W.-J. Hu, W. Zhu, Y. Zhang, S. Gong, F. Becca, and D. N. Sheng, *Phys. Rev. B* **91**, 041124(R) (2015).
- ³⁴ W.-J. Hu, S.-S. Gong, F. Becca, and D. N. Sheng, *Phys. Rev. B* **92**, 201105(R) (2015).
- ³⁵ Y. Iqbal, D. Poilblanc, and F. Becca, *Phys. Rev. B* **89**, 020407(R) (2014).
- ³⁶ T. Westerhout, N. Astrakhantsev, K. S. Tikhonov, M. Katsnelson, and A. A. Bagrov, *Nature Communications* **11**, 1593 (2020).
- ³⁷ C. Fu, X. Zhang, H. Zhang, H. Ling, S. Xu, and S. Ji, *arXiv:2206.07370*.
- ³⁸ D. Kochkov, T. Pfaff, A. Sanchez-Gonzalez, P. Battaglia, B. K. Clark, *arXiv:2110.06390*.
- ³⁹ L. Yang, W. Hu, L. Li, *arXiv:2011.12453*.
- ⁴⁰ J. B. Marston, and C. Zeng, *J. Appl. Phys.* **69**, 5962 (1991).
- ⁴¹ C. Zeng, and V. Elser, *Phys. Rev. B* **51**, 8318 (1995).
- ⁴² P. Nikolic, and T. Senthil, *Phys. Rev. B* **68**, 214415 (2003).
- ⁴³ R. R. P. Singh, and D. A. Huse, *Phys. Rev. B* **76**, 180407(R) (2007).
- ⁴⁴ R. R. P. Singh, and D. A. Huse, *Phys. Rev. B* **77**, 144415 (2008).
- ⁴⁵ D. Poilblanc, M. Mambrini, and D. Schwandt, *Phys. Rev. B* **81**, 180402(R) (2010).
- ⁴⁶ D. Schwandt, M. Mambrini, and D. Poilblanc, *Phys. Rev. B* **81**, 214413 (2010).
- ⁴⁷ D. Poilblanc, and A. Ralko, *Phys. Rev. B* **82**, 174424 (2010).
- ⁴⁸ K. Hwang, Y. B. Kim, J. Yu, and K. Park, *Phys. Rev. B* **84**, 205133 (2011).
- ⁴⁹ D. Poilblanc, and G. Misguich, *Phys. Rev. B* **84**, 214401 (2011).
- ⁵⁰ M. Hermele, Y. Ran, P. A. Lee, and X. G. Wen, *Phys. Rev. B* **77**, 224413 (2008).
- ⁵¹ O. Ma and J. B. Marston, *Phys. Rev. Lett.* **101**, 027204 (2008).
- ⁵² Y. Iqbal, F. Becca, and D. Poilblanc, *New J. Phys.* **14**, 115031 (2012).
- ⁵³ Y. Iqbal, F. Becca, S. Sorella, and D. Poilblanc, *Phys. Rev. B* **87**, 060405(R) (2013).
- ⁵⁴ C.-Y. Lee, B. Normand, and Y.-J. Kao, *Phys. Rev. B* **98**, 224414 (2018).
- ⁵⁵ G. Pan, and Z. Y. Meng, *arXiv:2204.08777*.
- ⁵⁶ M. Troyer and U.-J. Wiese, *Phys. Rev. Lett.* **94**, 170201 (2005).
- ⁵⁷ S. R. White, *Phys. Rev. B* **48**, 10345 (1993).
- ⁵⁸ S. R. White, *Phys. Rev. Lett.* **69**, 2863 (1992).
- ⁵⁹ U. Schollwöck, *Rev. Mod. Phys.* **77**, 259 (2005).
- ⁶⁰ U. Schollwöck, *Annals of Physics* **326**, 96 (2011).
- ⁶¹ G. K.-L. Chan, *Low entanglement wavefunctions*, Wiley Interdisciplinary Reviews: Computational Molecular Science, **2**(6), 907-920 (2012).
- ⁶² F. Ferrari, A. Parola, and F. Becca, *Phys. Rev. B* **103**, 195140 (2021).
- ⁶³ S. Hu, W. Zhu, S. Eggert, and Y.-C. He, *Phys. Rev. Lett.* **123**, 207203 (2019).
- ⁶⁴ W. Zhu, X. Chen, Y.-C. He, and W. Witczak-Krempa, *Science Advances* **4**, 11 (2018).
- ⁶⁵ G. Carleo, K. Choo, D. Hofmann, J. E. T. Smith, T. Westerhout, F. Alet, E. J. Davis, S. Efthymiou, I. Glasser, S.-H. Lin, M. Mauri, G. Mazzola, C. B. Mendl, E. van Nieuwenburg, O. O'Reilly, H. Théveniaut, G. Torlai, and A. Wietek, *SoftwareX* **10**, 100311 (2019).
- ⁶⁶ F. Vicentini, D. Hofmann, A. Szabó, D. Wu, C. Roth, C. Giuliani, G. Pescia, J. Nys, V. Vargas-Calderón, N. Astrakhantsev, and G. Carleo, *NetKet 3: Machine Learning Toolbox for Many-Body Quantum Systems*, *SciPost Phys. Codebases* **7** (2022); <https://www.netket.org/>.
- ⁶⁷ M. Abadi, A. Agarwal, P. Barham, E. Brevdo, Z. Chen, C. Citro, G. S. Corrado, A. Davis, J. Dean, M. Devin, S. Ghemawat, I. Goodfellow, A. Harp, G. Irving, M. Isard, Y. Jia, R. Jozefowicz, L. Kaiser, M. Kudlur, J. Levenberg, D. Mane, R. Monga, S. Moore, D. Murray, C. Olah, M. Schuster, J. Shlens, B. Steiner, I. Sutskever, K. Talwar, P. Tucker, V. Vanhoucke, V. Vasudevan, F. Viegas, O. Vinyals, P. Warden, M. Wattenberg, M. Wicke, Y. Yu, and X. Zheng, *TensorFlow: Large-Scale Machine Learning on Heterogeneous Distributed Systems*, 2015 (<https://www.tensorflow.org/>); *arXiv:1603.04467*.
- ⁶⁸ G. Carleo, and M. Troyer, *Science* **355**, 602 (2017).
- ⁶⁹ Z. Cai, and J. Liu, *Phys. Rev. B* **97**, 035116 (2018).
- ⁷⁰ X. Liang, W.-Y. Liu, P.-Z. Lin, G.-C. Guo, Y.-S. Zhang, and L. He, *Phys. Rev. B* **98**, 104426 (2018).
- ⁷¹ K. Choo, T. Neupert, and G. Carleo, *Phys. Rev. B* **100**, 125124 (2019).
- ⁷² F. Ferrari, F. Becca, and J. Carrasquilla, *Phys. Rev. B* **100**, 125131 (2019).
- ⁷³ O. Sharif, Y. Levine, N. Wies, G. Carleo, and A. Shashua, *Phys. Rev. Lett.* **124**, 020503 (2020).
- ⁷⁴ M. Hibat-Allah, M. Ganahl, L. E. Hayward, R. G. Melko, and J. Carrasquilla, *Phys. Rev. Research* **2**, 023358 (2020).
- ⁷⁵ A. Szabó and C. Castelnovo, *Phys. Rev. Research* **2**, 033075 (2020).
- ⁷⁶ Y. Nomura, and M. Imada, *Phys. Rev. X* **11**, 031034 (2021).

- ⁷⁷ N. Astrakhantsev, T. Westerhout, A. Tiwari, K. Choo, A. Chen, M. H. Fischer, G. Carleo, and T. Neupert, *Phys. Rev. X* **11**, 041021 (2021).
- ⁷⁸ Y. Nomura, *J. Phys.: Condens. Matter* **33**, 174003 (2021).
- ⁷⁹ M. Bukov, M. Schmitt, and M. Dupont, *SciPost Phys.* **10**, 147 (2021).
- ⁸⁰ C. Roth, and A. MacDonald, arXiv:2104.05085.
- ⁸¹ C. Roth, A. Szabó, and A. MacDonald, *Phys. Rev. B* **108**, 054410 (2023).
- ⁸² Y. Nomura, A. S. Darmawan, Y. Yamaji, and M. Imada, *Phys. Rev. B* **96**, 205152 (2017).
- ⁸³ D. Luo, and B. K. Clark, *Phys. Rev. Lett.* **122**, 226401 (2019).
- ⁸⁴ D. Pfau, J. S. Spencer, A. G. D. G. Matthews, and W. M. C. Foulkes, *Phys. Rev. Research* **2**, 033429 (2020).
- ⁸⁵ K. Choo, A. Mezzacapo, and G. Carleo, *Nat. Commun.* **11**, 2368 (2020).
- ⁸⁶ J. Stokes, J. R. Moreno, E. A. Pnevmatikakis, and G. Carleo, *Phys. Rev. B* **102**, 205122 (2020).
- ⁸⁷ G. Cassella, H. Sutterud, S. Azadi, N. D. Drummond, D. Pfau, J. S. Spencer, and W. M. C. Foulkes, *Phys. Rev. Lett.* **130**, 036401 (2023).
- ⁸⁸ H. J. Changlani, J. M. Kinder, C. J. Umrigar, and G. Kin-Lic Chan, *Phys. Rev. B* **80**, 245116 (2009).
- ⁸⁹ S. R. Clark, *J. Phys. A: Math. Theor.* **51** 135301 (2018).
- ⁹⁰ D.-L. Deng, X. Li, and S. Das Sarma, *Phys. Rev. B* **96**, 195145 (2017).
- ⁹¹ I. Glasser, N. Pancotti, M. August, I. D. Rodriguez, and J. I. Cirac, *Phys. Rev. X* **8**, 011006 (2018).
- ⁹² R. Kaubruegger, L. Pastori, and J. C. Budich, *Phys. Rev. B* **97**, 195136 (2018).
- ⁹³ S. Lu, X. Gao, and L.-M. Duan, *Phys. Rev. B* **99**, 155136 (2019).
- ⁹⁴ Y. Huang, and J. E. Moore, *Phys. Rev. Lett.* **127**, 170601 (2021).
- ⁹⁵ T. Vieijra, C. Casert, J. Nys, W. De Neve, J. Haegeman, J. Ryckebusch, and F. Verstraete, *Phys. Rev. Lett.* **124**, 097201 (2020).
- ⁹⁶ T. Vieijra, and J. Nys, *Phys. Rev. B* **104**, 045123 (2021).
- ⁹⁷ T. Đurić, and T. Ševa, *Phys. Rev. B* **102**, 085104 (2020).
- ⁹⁸ K. Choo, G. Carleo, N. Regnault, and T. Neupert, *Phys. Rev. Lett.* **121**, 167204 (2018).
- ⁹⁹ M. Schmitt, and M. Heyl, *Phys. Rev. Lett.* **125**, 100503 (2020).
- ¹⁰⁰ I. L. Gutiérrez, and C. B. Mendl, *Quantum* **6**, 627 (2022).
- ¹⁰¹ D. Hofmann, G. Fabiani, J. H. Mentink, G. Carleo, and M. A. Sentef, *SciPost Phys.* **12**, 165 (2022).
- ¹⁰² A. Nagy, and V. Savona, *Phys. Rev. Lett.* **122**, 250501 (2019).
- ¹⁰³ M. J. Hartmann, and G. Carleo, *Phys. Rev. Lett.* **122**, 250502 (2019).
- ¹⁰⁴ F. Vicentini, A. Biella, N. Regnault, and C. Ciuti, *Phys. Rev. Lett.* **122**, 250503 (2019).
- ¹⁰⁵ N. Yoshioka, and R. Hamazaki, *Phys. Rev. B* **99**, 214306 (2019).
- ¹⁰⁶ D. Luo, Z. Chen, J. Carrasquilla, and B. K. Clark, *Phys. Rev. Lett.* **128**, 090501 (2022).
- ¹⁰⁷ M. Reh, M. Schmitt, and M. Gärttner, *Phys. Rev. Lett.* **127**, 230501 (2021).
- ¹⁰⁸ N. Irikura, and Hiroki Saito, *Phys. Rev. Research* **2**, 013284 (2020).
- ¹⁰⁹ Y. Nomura, N. Yoshioka, and F. Nori, *Phys. Rev. Lett.* **127**, 060601 (2021).
- ¹¹⁰ T. Mizusaki and M. Imada, *Phys. Rev. B* **69**, 125110 (2004).
- ¹¹¹ T. Misawa, S. Morita, K. Yoshimi, M. Kawamura, Y. Motoyama, K. Ido, T. Ohgoe, M. Imada, and T. Kato, *Comp. Phys. Commun.* **235**, 447 (2019).
- ¹¹² K. Seki, T. Shirakawa, and S. Yunoki, *Phys. Rev. A* **101**, 052340 (2020).
- ¹¹³ M. Reh, M. Schmitt, and M. Gärttner, *Phys. Rev. B* **107**, 195115 (2023).
- ¹¹⁴ D. Luo, Z. Chen, K. Hu, Z. Zhao, V. M. Hur, and B. K. Clark, *Phys. Rev. Research* **5**, 013216 (2023).
- ¹¹⁵ D. Luo, G. Carleo, B. K. Clark, and J. Stokes, *Phys. Rev. Lett.* **127**, 276402 (2021).
- ¹¹⁶ M. M. Bronstein, J. Bruna, T. Cohen, and P. Veličković, arXiv:2104.13478 (2021).
- ¹¹⁷ T. Cohen and M. Welling, *Group equivariant convolutional networks*, Proceedings of the International Conference on Machine Learning (ICML) (2016); arXiv:1602.07576.
- ¹¹⁸ R. Frostig, M. J. Johnson, and C. Leary, *Compiling machine learning programs via high-level tracing*, Systems for Machine Learning (2018).
- ¹¹⁹ J. Heek, A. Levskaya, A. Oliver, M. Ritter, B. Rondepierre, A. Steiner, and M. van Zee, *Flax: A neural network library and ecosystem for JAX*, <http://github.com/google/flax> (2020).
- ¹²⁰ M. Hessel, D. Budden, F. Viola, M. Rosca, E. Sezener, and T. Hennigan, *Optax: composable gradient transformation and optimisation, in jax!*, <http://github.com/deepmind/optax> (2020).
- ¹²¹ D. F. Agterberg, J.C. Séamus Davis, S. D. Edkins, E. Fradkin, D. J. Van Harlingen, S. A. Kivelson, P. A. Lee, L. Radzihovskiy, J. M. Tranquada, and Y. Wang, *Annual Review of Condensed Matter Physics, The Physics of Pair-Density Waves: Cuprate Superconductors and Beyond*, Vol. 11:231-270 (2020).
- ¹²² P. A. Lee, *Phys. Rev. X* **4**, 031017 (2014).
- ¹²³ S.-S. Lee, P. A. Lee, and T. Senthil, *Phys. Rev. Lett.* **98**, 067006 (2007).
- ¹²⁴ X. Y. Xu, K. T. Law, and P. A. Lee, *Phys. Rev. Lett.* **122**, 167001 (2019).
- ¹²⁵ D. Chakraborty, and A. M. Black-Schaffer, *New J. Phys.* **23**, 033001 (2021).
- ¹²⁶ Y. LeCun, Y. Bengio, and G. Hinton, *Nature* **521**, 436 (2015).
- ¹²⁷ I. Goodfellow, Y. Bengio, and A. Courville, *Deep learning* (MIT press, Cambridge, MA, 2016).
- ¹²⁸ John D. Kelleher, *Deep learning* (MIT press, Cambridge, MA, 2019).
- ¹²⁹ R. Kondor, and S. Trivedi, *On the generalization of equivariance and convolution in neural networks to the action of compact groups*, Proceedings of the 35th International Conference on Machine Learning (ICML)(2018); arXiv:1802.03690.
- ¹³⁰ G. Klambauer, T. Unterthiner, A. Mayr, and S. Hochreiter, *Self-Normalizing Neural Networks*, Advances in Neural Information Processing Systems 30 (NIPS 2017); arXiv:1706.02515.
- ¹³¹ V. Heine, *Group Theory in Quantum Mechanics*, (Dover, 2007).
- ¹³² M.S. Dresselhaus, G. Dresselhaus, and A. Jorio, *Group Theory - Application to the Physics of Condensed Matter* (Springer-Verlag Berlin Heidelberg, 2008).
- ¹³³ S. Sorella, *Phys. Rev. Lett.* **80**, 4558 (1998).
- ¹³⁴ S. Sorella, *Phys. Rev. B* **64**, 024512 (2001).

- ¹³⁵ S. Sorella, M. Casula, and D. Rocca, *J. Chem. Phys.* **127**, 014105 (2007).
- ¹³⁶ F. Becca and S. Sorella, *Quantum Monte Carlo Approaches for Correlated Systems* (Cambridge University Press, Cambridge, 2017).
- ¹³⁷ D. P. Kingma and J. Ba, Adam: *A Method for Stochastic Optimization*, 3rd International Conference for Learning Representations (San Diego, 2015); arXiv:1412.6980.
- ¹³⁸ S.-i. Amari, *Neural Computation* **10**, 251 (1998).
- ¹³⁹ H. Park, and K. Lee, *Appl. Sci.* **9**(21), 4568 (2019).
- ¹⁴⁰ J. Martens, *J. Mach. Learn. Res.* **21**, 146:1-146:76 (2020).
- ¹⁴¹ S. Dong, F. Le, M. Zhang, S.-J. Tao, C. Wang, Y.-J. Han, and G.-P. Guo, arXiv:2210.02764.
- ¹⁴² C.-Y. Park, and M. J. Kastoryano, *Phys. Rev. Research* **2**, 023232 (2020).
- ¹⁴³ J. Stokes, J. Izaac, N. Killoran, and G. Carleo, *Quantum* **4**, 269 (2020).
- ¹⁴⁴ C. Roth, arXiv:2003.06228.
- ¹⁴⁵ D. Wu, L. Wang, and P. Zhang, *Phys. Rev. Lett.* **122**, 080602 (2019).
- ¹⁴⁶ M. Hibat-Allah, E. M. Inack, R. Wiersema, R. G. Melko, and J. Carrasquilla, *Nature Machine Intelligence* **3**, 952–961 (2021).
- ¹⁴⁷ M. Hibat-Allah, R. G. Melko, and J. Carrasquilla, *Supplementing Recurrent Neural Network Wave Functions with Symmetry and Annealing to Improve Accuracy*, Machine Learning and the Physical Sciences Workshop (NeurIPS 2021); arXiv:2207.14314.
- ¹⁴⁸ T. M. Cover, and J. A. Thomas, *Elements of information theory* (Wiley, New York, 1991).
- ¹⁴⁹ L. Gioia, and C. Wang, *Phys. Rev. X* **12**, 031007 (2022).
- ¹⁵⁰ M. I. Aroyo, *International Tables for Crystallography, Volume A: Space-group Symmetry* (Wiley, New York, 2016).
- ¹⁵¹ R. Bamler, and S. Mandt, *Improving Optimization for Models With Continuous Symmetry Breaking*, Proceedings of the 35th International Conference on Machine Learning (ICML 2018), in PMLR 80:423-432; arXiv:1803.03234.
- ¹⁵² M. Barkeshli, H. Yao, and S. A. Kivelson, *Phys. Rev. B* **87**, 140402(R) (2013).
- ¹⁵³ X. - G. Wen, *Phys. Rev. B* **65**, 165113 (2002).
- ¹⁵⁴ Y.- M. Lu, Y. Ran, and P. A. Lee, *Phys. Rev. B* **83**, 224413 (2011).
- ¹⁵⁵ Y.- M. Lu, *Phys. Rev. B* **97**, 094422 (2018).
- ¹⁵⁶ M. B. Hastings, *Phys. Rev. B* **63**, 014413 (2000).
- ¹⁵⁷ Y. Iqbal, D. Poilblanc, and F. Becca, *Phys. Rev. B* **91**, 020402(R) (2015).
- ¹⁵⁸ Y. Iqbal, D. Poilblanc, R. Thomale, and F. Becca, *Phys. Rev. B* **97**, 115127 (2018).
- ¹⁵⁹ P. Fulde and R. A. Ferrell, *Phys. Rev.* **135**, A550 (1964).
- ¹⁶⁰ A. I. Larkin, and Yu. N. Ovchinnikov, *Sov. Phys. JETP* **20**, 762 (1965).
- ¹⁶¹ A. Kitaev, *Ann. Phys.* **321**, 2 (2006).
- ¹⁶² E. Berg, C.-C. Chen, and S. A. Kivelson, *Phys. Rev. Lett.* **100**, 027003 (2008).
- ¹⁶³ F. Loder, A. P. Kampf, and T. Kopp, *Phys. Rev. B* **81**, 020511(R) (2010).
- ¹⁶⁴ E. Fradkin, S. A. Kivelson, and J. M. Tranquada, *Rev. Mod. Phys.* **87**, 457 (2015).
- ¹⁶⁵ E. Berg, E. Fradkin, S. A. Kivelson, and J. Tranquada, *New J. Phys.* **11**, 115004 (2009).
- ¹⁶⁶ D. F. Agterbergand, and H. Tsunetsugu, *Nature Physics* **4**, 639–642 (2008).
- ¹⁶⁷ E. Berg, E. Fradkin, and S. A. Kivelson, *Nature Phys.* **5**, 830–833 (2009).
- ¹⁶⁸ D. F. Agterberg, and J. Garaud, *Phys. Rev. B* **91**, 104512 (2015).
- ¹⁶⁹ Y. Wang, S. D. Edkins, M. H. Hamidian, J. C. Séamus Davis, E. Fradkin, and S. A. Kivelson, *Phys. Rev. B* **97**, 174510 (2018).
- ¹⁷⁰ Z. Dai, Y.-H. Zhang, T. Senthil, and P. A. Lee, *Phys. Rev. B* **97**, 174511 (2018).
- ¹⁷¹ E. Berg, E. Fradkin, and S. A. Kivelson, *Phys. Rev. B* **79**, 064515 (2009).
- ¹⁷² L. Radzihovsky, and A. Vishwanath, *Phys. Rev. Lett.* **103**, 010404 (2009).
- ¹⁷³ D. Kiese, F. Ferrari, N. Astrakhantsev, N. Niggemann, P. Ghosh, T. Müller, R. Thomale, T. Neupert, J. Reuther, M. J. P. Gingras, S. Trebst, and Y. Iqbal, *Phys. Rev. Research* **5**, L012025 (2023).
- ¹⁷⁴ W.-H. Ko, P. A. Lee, and X.-G. Wen, *Phys. Rev. B* **79**, 214502 (2009).